



**HAL**  
open science

## Detailed investigation of two high-speed evolved Galactic stars

Aroa del Mar Matas Pinto, Elisabetta Caffau, Patrick François, Monique Spite, Piercarlo Bonifacio, Shinya Wanajo, Wako Aoki, Lorenzo Monaco, Takuma Suda, François Spite, et al.

► **To cite this version:**

Aroa del Mar Matas Pinto, Elisabetta Caffau, Patrick François, Monique Spite, Piercarlo Bonifacio, et al.. Detailed investigation of two high-speed evolved Galactic stars. *Astronomical Notes / Astronomische Nachrichten*, 2022, 343, 10.1002/asna.20210032 . insu-03719746

**HAL Id: insu-03719746**

**<https://insu.hal.science/insu-03719746>**

Submitted on 12 Oct 2022

**HAL** is a multi-disciplinary open access archive for the deposit and dissemination of scientific research documents, whether they are published or not. The documents may come from teaching and research institutions in France or abroad, or from public or private research centers.

L'archive ouverte pluridisciplinaire **HAL**, est destinée au dépôt et à la diffusion de documents scientifiques de niveau recherche, publiés ou non, émanant des établissements d'enseignement et de recherche français ou étrangers, des laboratoires publics ou privés.

**ARTICLE TYPE****Detailed investigation of two high-speed evolved Galactic stars<sup>†</sup>**A. M. Matas Pinto<sup>\*1</sup> | E. Caffau<sup>1</sup> | P. François<sup>2,3</sup> | M. Spite<sup>1</sup> | P. Bonifacio<sup>1</sup> | S. Wanajo<sup>4,5</sup> | W. Aoki<sup>6</sup> | L. Monaco<sup>7</sup> | T. Suda<sup>8,9</sup> | F. Spite<sup>1</sup> | L. Sbordone<sup>10</sup> | L. Lombardo<sup>1</sup> | A. Mucciarelli<sup>11,12</sup><sup>1</sup>GEPI, Observatoire de Paris, Université PSL, CNRS, 5 Place Jules Janssen, 92190 Meudon, France<sup>2</sup>GEPI, Observatoire de Paris, Université PSL, CNRS, 77 Av. Denfert-Rochereau, 75014 Paris, France<sup>3</sup>UPIV, Université de Picardie Jules Verne, 33 rue St Leu, 80080 Amiens, France<sup>4</sup>Max Planck Institute for Gravitational Physics (Albert Einstein Institute), Am Mühlenberg 1, Potsdam-Golm, 14476, Germany<sup>5</sup>iTHEMS Research Group, RIKEN, Wako, Saitama 351-0198, Japan<sup>6</sup>National Observatory of Japan, 2-21-1 Osawa, Mitaka, Tokyo 181-8588, Japan<sup>7</sup>Universidad Andres Bello, Departamento de Ciencias Fisicas, Fernandez Concha 700, Las Condes, Santiago, Chile<sup>8</sup>Department of Liberal Arts, Tokyo University of Technology, 5-23-22 Kamata, Ota-ku, Tokyo 144-8535, Japan<sup>9</sup>Research Center for the Early Universe, The University of Tokyo, 7-3-1 Hongo, Bunkyo-ku, Tokyo 113-0033, Japan<sup>10</sup>ESO - European Southern Observatory, Alonso de Cordova 3107, Vitacura, Santiago, Chile

Dipartimento di Fisica e Astronomia, Università degli Studi di Bologna, Via Gobetti 93/2, I-40129 Bologna, Italia

<sup>12</sup>INAF - Osservatorio di Astrofisica e Scienza dello Spazio di Bologna, Via Gobetti 93/3, I-40129 Bologna, Italy**Correspondence**

\*Corresponding author name, This is sample corresponding address. Email: authorone@gmail.com

**Present Address**

This is sample for present address text this is sample for present address text

The study of metal poor stars provides clarification and knowledge about the primordial Universe. Specially, halo stars provide explanations of the nature of the first generations of stars and the nucleosynthesis in the metal-poor regime. We present a detailed chemical analysis and determination of the kinematic and orbital properties of two stars characterised by high speed with respect to the Sun. We analysed two high-resolution Subaru spectra employing the MyGIsFOS code which allows to derive the detailed chemical abundances for 28 elements (C, N, O, Na, Mg, Al, Si, Ca, Sc, Ti, V, Cr, Mn, Fe, Co, Ni, Cu, Zn, Sr, Y, Zr, Ba, La, Ce, Pr, Nd, Sm, Eu), and abundance from two ionisation states in the case of four elements (Ti, Cr, Fe and Zr). TYC 622–742–1 and TYC 1193–1918–1 are metal-poor stars ([Fe/H] of  $-2.37$  and  $-1.60$ ), they are similar in the chemical pattern with respect to Fe, they are  $\alpha$  enhanced and show a slight excess in Eu abundance. Both giant stars are poor in C and rich in N, as expected for evolved stars, and this fact is supported by the low  $^{12}\text{C}/^{13}\text{C}$  isotopic ratio in TYC 1193–1918–1. Nevertheless, the C abundance of TYC 622–742–1 is particularly low. TYC 622–742–1 and TYC 1193–1918–1 have a similar chemical composition to the other Galactic halo stars of comparable metallicity. According to their kinematics, both stars belong to the Galactic halo, but they are not a part of the Gaia-Sausage-Enceladus structure.

**KEYWORDS:**

Stars: abundances - Galaxy: abundances - Galaxy: evolution - Galaxy: formation - Galaxy: kinematics and dynamics - Galaxy: halo

**1 | INTRODUCTION**

The old, metal-poor stellar population provides us information about the Universe in its infancy. In fact, the majority of metal-poor stars have an age comparable to the age of the Universe

<sup>†</sup>Based on observations made with HDS at Subaru.

(see e.g. Cayrel et al., 2001), so their chemical pattern reflects the chemical composition of the primordial Universe. These stars were born at a time when just one/few generations of massive stars had a chance to explode as supernovae and enrich the interstellar gas from where they formed. Metal-poor stars are rare, overall in the solar vicinity, meaning the part of the Galaxy accessible for high-resolution and high signal-to-noise spectroscopy.

In the recent years two methods have mainly been used to select metal-poor candidates: (i) from low-resolution spectroscopy (see e.g. Christlieb et al., 2004); (ii) from narrow-band photometry (see e.g. Caffau et al., 2020b). Broad-band photometry (iii) also allowed to select metal-poor candidates, albeit with a lower success rate (Schlaufman & Casey, 2014).

(i) Several low-resolution spectroscopic surveys collected large numbers of spectra from where metallicity and sometimes abundances for other elements could be derived. We here recall some very efficient surveys that allowed to find extremely metal-poor stars.

1. A list of weak-metal stars is provided by Bidelman & MacConnell (1973, see their Table V) from their objective prism survey.
2. The Bond survey (Bond, 1970) was based on objective prism observations at depth of  $B \sim 10 - 10.5$  when the telescope used was at the University of Michigan, becoming  $B \sim 11.5$  when the telescope was moved at Cerro Tololo in 1976. The result of this survey was presented in Bond (1980).
3. The HK Survey (Beers et al., 1985) observed with objective prism stars in a way to collect a kinematically unbiased sample of metal-poor stars. This survey allowed to discover the extremely metal-poor binary system CS 22876–032 (see Beers et al., 1985); the extremely metal-poor star CS 31082–001 with Th and U detectable (see Cayrel et al., 2001); to collect the stellar sample of metal-poor stars observed in the ESO large programme “First Stars” (Cayrel et al., 2004) and usually used as the reference metal-poor sample.
4. The Hamburg-ESO survey (Christlieb et al. 2000, Christlieb et al. 2008), conceived to discover quasars, allowed to find out a large number of metal-poor stars (see e.g. Christlieb et al., 2002).
5. The Sloan Digital Sky Survey (SDSS York et al., 2000) in the latest 20 years provided low-resolution spectra for a large number of metal-poor candidates, whose low metallicity has been confirmed at high-resolution investigation (see e.g. Aguado et al., 2018; Matsuno et al., 2017). In this context, the TOPoS project selected from the SDSS

spectral database the stars with turn off colours and analysed the spectra with an independent pipeline (see Caffau et al., 2013). Several EMP stars have been discovered in this project (see Bonifacio et al. 2015, Caffau et al. 2016, Bonifacio et al. 2018).

6. The Large Sky Area Multi-Object fiber Spectroscopic Telescope (LAMOST Cui et al., 2012) provided a large amount of stellar spectra that allowed to discover (see e.g. Li et al. 2015a, Li et al. 2018) and then also confirm with a high-resolution follow-up (see e.g. Li et al., 2015b), many metal-poor stars.
7. The Radial Velocity Experiment (RAVE Steinmetz et al., 2006) allowed to select a large sample of metal-poor stars (see e.g. Matijević et al., 2017).

(ii) The narrow-band photometry allows to observe a much larger number of stars with respect to the low-resolution spectroscopic surveys, but an efficient calibration is necessary in order to select interesting candidates.

1. The SkyMapper Telescope (Keller et al., 2007) observes also with an intermediate-band filter (about 40 nm FWHM) centred on the Ca II-H and -K lines. Several metal-poor candidates selected from the SkyMapper Survey (Wolf et al., 2018) have been confirmed from high-resolution spectroscopy to be extremely metal-poor stars (see e.g. Jacobson et al., 2015).
2. The Pristine survey (Starkenburg et al., 2017) is a photometric campaign observing with a narrow-band (about 20 nm FWHM) filter centred at the Ca II-H and -K lines. It is a very efficient project, allowing to select metal-poor candidates whose low-metallicity has been confirmed on high-resolution spectroscopy (see e.g. Starkenburg et al., 2018).
3. The S-plus survey (Mendes de Oliveira et al., 2019) uses several wide bands and narrow bands, among which J0395, centred on the Ca II-H and -K lines and has been successfully used to select metal-poor candidates (Placco et al. 2021, Whitten et al. 2021, Monaco et al., in preparation).
4. The J-plus survey uses a similar telescope and filter set as S-plus (Cenarro et al., 2019) and has also been able to select some metal-poor stars (Andrés Galarza et al., 2021).

(iii) Schlaufman & Casey (2014) used the photometric data from APASS (Henden et al., 2009), 2MASS and WISE to select metal-poor candidates and confirmed by follow-up spectroscopy that 3.8% of the candidates had  $[\text{Fe}/\text{H}] \lesssim -3$ .

Metal-poor stars have long been known, before surveys provided us with large numbers of low-resolution spectra and narrow-band photometry were available. Seventy years ago, Chamberlain & Aller (1951) analysed two stars (HD 19445 and HD 140283), nowadays denoted as the prototype of metal-poor stars. From the weak lines in their spectra, Chamberlain & Aller (1951) adopted a model of an F-type sub-dwarf to investigate them and claim a low abundance of Ca and Fe. Schwarzschild & Schwarzschild (1950) divided a sample of nine F stars in high- and low-velocity, and in their Figure 4 one can see that the high-velocity stars show generally smaller strength on the Fe I lines. Roman (1950) realised that stars of the same spectral type can have spectral lines of different strength. Dividing the stars in two groups, according to the strength of the spectral lines, she investigated the stellar velocity, concluding that the star with weak metallic lines have larger velocities and a larger dispersion in velocity. In Roman (1955), a catalogue of high-speed stars is provided, and the two metal-poor prototype stars by Chamberlain & Aller (1951) are in. This suggests that selecting the high-velocity stars is a way to select metal-poor stars. In fact, stars that show a high velocity with respect to the Sun surely have an orbit widely different from the solar one so these stars cannot belong to the Galactic disc but, if bound, these are Halo stars. The stars indicated as “high proper-motion” or “high-velocity” star have kinematic non-compatible with the Galactic disc. This is not obviously translated in extreme kinematic with respect to the centre of the Galaxy.

Thanks to the Gaia mission data (Gaia Collaboration et al., 2016), for a large number of stars it is presently possible to derive accurate kinematical and orbital parameters. Gaia catalogues also allow us to select stars with specific kinematics. In Caffau et al. (2020a), we selected a sample of high-speed stars to be observed at low-resolution. We derived chemical abundances for a few elements and deduced that the selected stars are mainly Halo stars, with a very homogeneous chemistry. From low-resolution spectroscopy, determination of the chemical pattern is very limited. We then decided to take the advantage of the Subaru large telescope to secure high-quality spectra for two bright stars characterised by high speed with respect to the Sun.

We here investigate the detailed chemical pattern of these two stars to see if they show any peculiarity.

## 2 | TARGET SELECTION AND OBSERVATIONS

The two targets were part of a set of bright stars we selected as backup for our observing run at Subaru. The selection criterion was based on Gaia DR2 requiring  $G < 11$  and total speed

with respect to the Sun  $> 500 \text{ km s}^{-1}$ . The observations were carried out on September 13th 2019 with the High Dispersion Spectrograph (HDS) installed on the Subaru telescope atop the Mauna Kea volcano in Hawaii (Noguchi et al., 2002). The bad weather conditions did not permit to perform the main programme on faint targets. Instead, the two stars analysed in this article were selected in the list of the backup programme. The wavelength coverage goes from 408.4 nm to 689.2 nm. A binning  $2 \times 2$  has been adopted leading to a resolving power of about 40000. The log of the observations is given in Table 1. Standard data reduction procedures were carried out with the IRAF Echelle package<sup>1</sup>.

To show the quality of the spectra, in Fig. 1 the range of the 664 nm Eu II line is plotted.

## 3 | ANALYSIS

### 3.1 | Radial velocity and kinematics

The radial velocity is measured finding the maximum of the cross-correlation function (Tonry & Davis, 1979). As the template we employed a synthetic spectrum with the stellar parameters adopted for each star. Table 3 shows the radial velocity of the two stars and their statistical uncertainties that reflects the S/N ratio of the spectrum. We report a radial velocity of  $-115.1 \pm 1.1 \text{ km s}^{-1}$  for TYC 622-742-1 and  $-365.2 \pm 0.9 \text{ km s}^{-1}$  for TYC 1193-1918-1 (see Table 3). The statistical error in the radial velocity determination is  $\sim 1.0 \text{ km s}^{-1}$ . For the two stars Gaia DR2 provide a radial velocity of  $-114.0 \pm 0.4$  for TYC 622-742-1 and  $-364.3 \pm 0.3$  for TYC 1193-1918-1 (see Gaia Collaboration et al., 2018). The radial velocities we derive are compatible, within uncertainties, with the values provided by Gaia DR2.

We derived the zero-point for the parallax as described in Lindgren et al. (2021). The parallax corrected for the zero-point has been used to derive the stellar and orbital parameters.

The orbital parameters have been derived using the Galpy code<sup>2</sup> together with the MWPotential14 potential (Bovy, 2015). We used the Gaia EDR3 coordinates, proper motions and zero-point corrected parallax and the radial velocities we measured. We adopted the solar motions of Schönrich et al. (2010) and the solar distance from the galactic centre of 8 kpc. In order to estimate the uncertainties on the derived quantities, we followed the same approach of Bonifacio et al. (2021). In particular, we used the pyia code<sup>3</sup> (Price-Whelan, 2018) to perform one thousand extractions of the six Galpy input

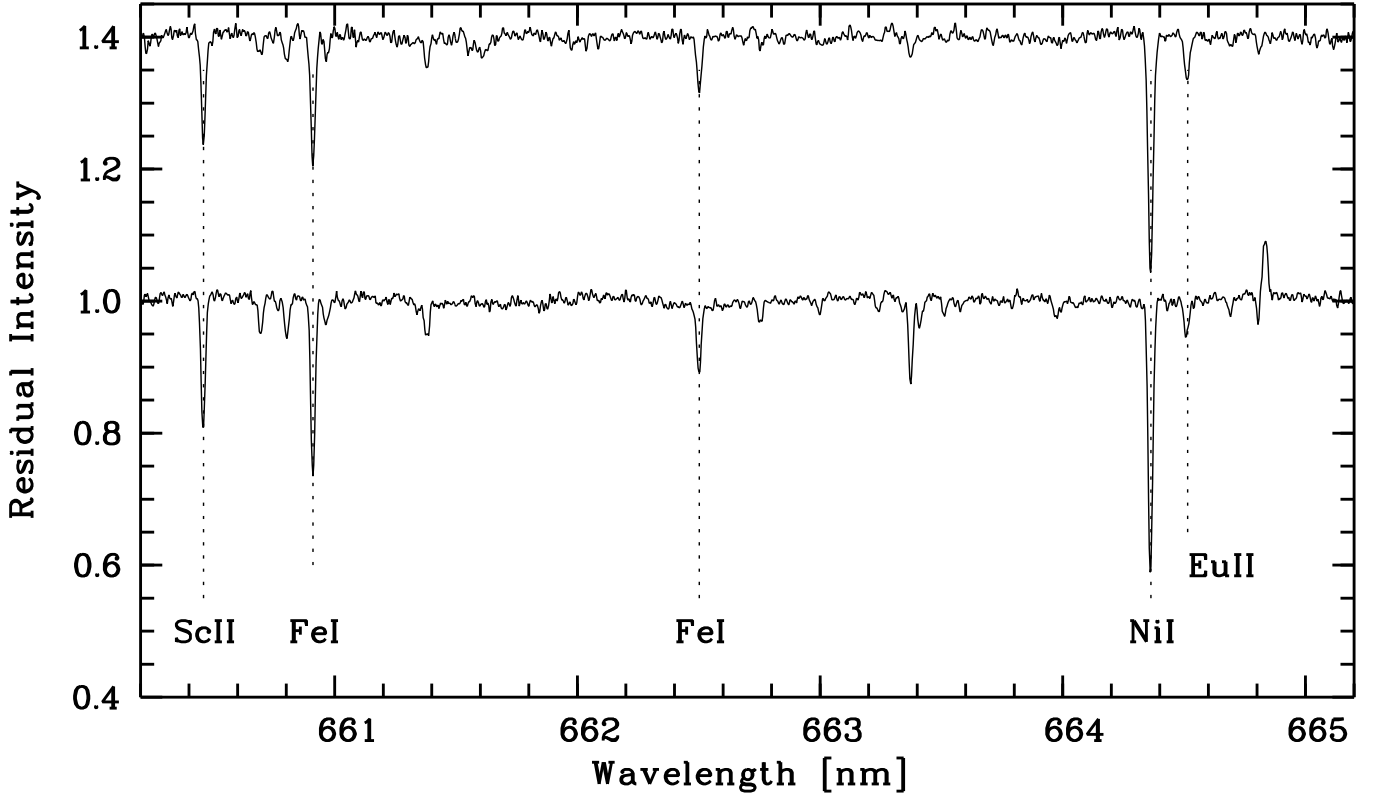
<sup>1</sup>IRAF is distributed by the National Optical Astronomy Observatories, which is operated by the Association of Universities for Research in Astronomy, Inc. under cooperative agreement with the National Science Foundation

<sup>2</sup><http://github.com/jobovy/galpy>

<sup>3</sup><https://github.com/adrn/pyia>

**TABLE 1** Observation log

Object	V mag	Observation date yyyy-mm-dd	Observation time UT	Exp. time s	S/N @ 480 nm
TYC 622-742-1	11.54	2019-09-13	13:04	600	200
TYC 1193-1918-1	10.70	2019-09-13	12:47	600	250

**FIGURE 1** The two spectra are here shown in the range of the Eu II line.

parameters from a multivariate Gaussian which takes into account both the errors on the parameters and their correlation coefficients in the construction of the covariance matrix. For each realisation, an orbit integration is then performed using Galpy. We adopted as uncertainties, the standard deviations of the calculated orbital parameters (see Table 4 ).

### 3.2 | Stellar parameters

We derived the stellar parameters from the photometry and parallax of the Gaia EDR3 catalogue (Gaia Collaboration et al., 2021, see Table 2 ). We dereddened the Gaia photometry ( $G$  and  $G_{BP} - G_{RP}$ ) by using the maps by Schlafly & Finkbeiner (2011). The parallax, after application of the zero-point, allowed us to derive the absolute  $G$  magnitude and then to derive the surface gravity by using the Stefan-Boltzmann

equation<sup>4</sup>. We adopted for both stars a mass of  $0.8 M_{\odot}$  (see e.g. Bonifacio et al., 2019), a typical value for old stars now on the red giant branch (RGB). A change in the initial mass would affect the stellar parameters but well within the uncertainties:  $\pm 0.1 M_{\odot}$  difference provides a change within about 10 K in effective temperature ( $T_{\text{eff}}$ ) and 0.05 dex in the surface gravity ( $\log g$ ). By comparing  $(G_{BP} - G_{RP})_0$  to the theoretical colour, we could derive the effective temperature. We assumed a metallicity  $[\text{Fe}/\text{H}] = -1.0$  for the first guess parameters.

The process provides us with initial values for stellar parameters. These initial parameters have been assigned as input to

<sup>4</sup>We use it in the form  $\log g = \log(M) + 4 \log(T_{\text{eff}}/5777) + 0.4(G + BCG) + 2 \log \varpi + 0.11 + 4.4377$  where  $M$  is the mass of the star in units of solar masses,  $G$  is the Gaia magnitude of the star,  $BCG$  is the bolometric correction in the  $G$  band,  $\varpi$  is the parallax, 5777 is the effective temperature of the Sun, 4.4377 is  $\log g$  of the Sun and 0.11 is a constant linked to the absolute bolometric magnitude of the Sun. See Nissen et al. (1997) for a derivation of this form of the formula.

**TABLE 2** Gaia eDR3 data.

	TYC 622–742–1	TYC 1193–1918–1
RA	01:50:23.07	00:40:48.26
Dec	+08:14:31.7	+20:52:17.5
Parallax (p)	0.1693	0.5726
$\sigma p$	0.0153	0.0156
p zero-point	–0.032	–0.035
pmRA	13.496	13.142
pmDec	–4.5610	–46.7576
Gmag	10.996	10.323
$G_{BP}$	11.765	10.859
$G_{RP}$	10.142	9.626
$V_r$ [km/s]	–114.0	–364.3
$\sigma V_r$ [km/s]	0.4	0.3

**TABLE 3** Radial velocities.

Star	$V_r$	$\sigma V_r$
TYC	km s <sup>–1</sup>	km s <sup>–1</sup>
TYC 622–742–1	–115.1	1.1
TYC 1193–1918–1	–365.2	0.9

**TABLE 4** Target stars kinematical parameters.

	TYC 622–742–1	TYC 1193–1918–1
$V_R$ (km s <sup>–1</sup> )	–108 ± 11	–226 ± 3
$V_T$ (km s <sup>–1</sup> )	–98 ± 25	–234 ± 6
$V_Z$ (km s <sup>–1</sup> )	108 ± 1	–24 ± 7
$R_{apo}$ (kpc)	13 ± 2	31 ± 2
$R_{peri}$ (kpc)	7 ± 1	5.3 ± 0.1
e	0.32 ± 0.05	0.70 ± 0.01
$Z_{max}$ (kpc)	11 ± 1	5 ± 1
E (km <sup>2</sup> s <sup>–2</sup> )	–31831±5155	–8178±2323
$L_Z$ (kpc km s <sup>–1</sup> )	–1047±290	–2026±55
$J_R$ (kpc km s <sup>–1</sup> )	136±39	1265±117

the pipeline MyGIsFOS (Sbordone et al., 2014, see Sec. 3.3 for explanations) to derive the stellar metallicity. The metallicity provided by MyGIsFOS was used to derive new stellar parameters. The process was iterated up to when the variation in effective temperature and surface gravity were negligible (less than a few K for  $T_{\text{eff}}$  and below 0.01 dex for  $\log g$ ). In this way we derived the final  $T_{\text{eff}}$  and  $\log g$  for the two stars that are the adopted stellar parameters, used for the chemical investigation and listed in Table 5 .

The uncertainty in the  $G_{BP}$  and  $G_{RP}$  bands brings a very small variation in  $T_{\text{eff}}$ . But, as a sanity check, we derived the stellar parameters in other three ways.

- We used the calibration of Mucciarelli et al. (2021), based on the Infrared Flux Method temperatures of González Hernández & Bonifacio (2009), and derived  $T_{\text{eff}}$  about 10 and 100 K hotter for TYC 622–742–1 and TYC 1193–1918–1, respectively.
- We allow MyGIsFOS to derive the stellar parameters (all free) and obtained, for TYC 622–742–1:  $T_{\text{eff}} = 4187 \pm 30$  K,  $\log g = 0.20 \pm 0.06$  (which is a value extrapolated in the grid),  $\xi = 1.96 \pm 0.05$  km s<sup>–1</sup> and for TYC 1193–1918–1:  $T_{\text{eff}} = 4650 \pm 30$  K,  $\log g = 1.59 \pm 0.05$ ,  $\xi = 1.56 \pm 0.03$  km s<sup>–1</sup>. So an extremely good agreement with the adopted parameters is obtained for both stars.
- The dereddened Gaia DR3 photometry is compared to PARSEC isochrones (Bressan et al., 2012; Marigo et al., 2017, see Fig. 2 ) coloured with the Gaia photometry in the colour-magnitude diagram ( $G_{BP} - G_{RP}$ ,  $G_{abs}$ ), by using metallicity of –1.5 and –1.0, respectively, for the two stars, and by adopting an age of 12 Gyr. The derived stellar parameters are: 4268 K and 0.71 for TYC 622–742–1 and 4621 K and 1.75 for TYC 1193–1918–1. For both stars, the agreement with the adopted parameters is excellent.

The uncertainties in parallax are non negligible for the two stars (see Table 2 ). We then checked what happens to  $\log g$  when we add/subtract the uncertainty to the parallax and if we apply or do not apply the zero-point. We derived changes of about 0.08 dex in  $\log g$ .

In a conservative way, we adopt an uncertainty of 100 K for the effective temperature and 0.2 dex for the surface gravity.

For the micro-turbulence, we see two obvious calibrations that could be applied.

- Monaco et al. (2005) derived a calibration for Sgr stars. One of the two stars here investigated, TYC 1193-1918-1, has a metallicity comparable with the Sgr sample by Monaco et al. (2005), while the other is about 0.5 dex more metal-poor. For the two stars, by using this calibration, we derive a micro-turbulence of 2.04 and 1.71 km s<sup>–1</sup>, respectively.
- With the calibration provided by Mashonkina et al. (2017), we derive a micro-turbulence of 2.07 and 1.74 km s<sup>–1</sup>, respectively, for our stars.

The two calibrations provide micro-turbulence in close agreement, and also compatible with the values provided by MyGIsFOS. MyGIsFOS is able to derive the micro-turbulence by

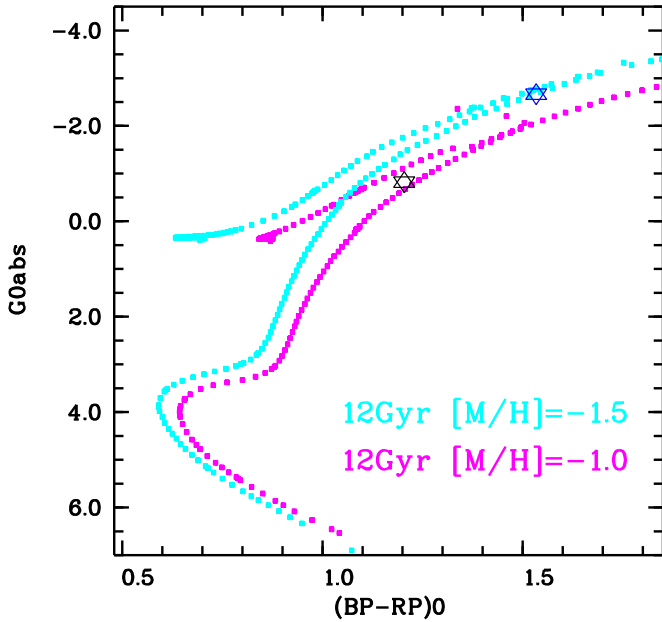


**FIGURE 2** The two observed stars (blue TYC 622–742–1 and black TYC 1193–1918–1) in the colour-magnitude diagram, compared to 12 Gyr PARSEC isochrones.

equalising the Fe abundance derived from selected, cleaned Fe I lines of different strength. Since the spectra are of good quality and we have several suitable Fe I lines, we decided to adopt these values for the microturbulence. In this way we derived a micro-turbulence of  $2.00 \pm 0.05 \text{ km s}^{-1}$  for TYC 622–742–1 and of  $1.52 \pm 0.03 \text{ km s}^{-1}$  for TYC 1193–1918–1, values reported in Table 5. In the case of TYC 622–742–1, the value is about  $0.20 \text{ km s}^{-1}$  smaller than the value derived by using the calibration by Mashonkina et al. (2017) or by Monaco et al. (2005), while in the case of TYC 1193–1918–1 all the values are very close, within the uncertainty derived by MyGIsFOS. The uncertainties provided by MyGIsFOS are just statistic, while, comparing the adopted values with the ones derived from calibrations, we can assume an uncertainty of  $0.2 \text{ km s}^{-1}$  for the micro-turbulence.

### 3.3 | Abundance determination

With the adopted stellar parameters, the observed spectra have been analysed with MyGIsFOS to derive the metallicity and the detailed chemical abundances. As described by Sbordone et al. (2014), MyGIsFOS is a pipeline that interpolates in a pre-computed grid of synthetic spectra to find the best fit spectrum for each feature analysed. The grid of synthetic spectra, based on ATLAS 12 models (Kurucz, 2005), was computed with SYNTHE (Kurucz, 2005). The grid we used has:  $T_{\text{eff}}$  in the range 4000–5200 K with a 200 K step;  $\log g$  from 0.5 to 3.0 with a 0.5 dex step; metallicity from  $-3.0$  to  $-0.5$  with 0.5 dex

step; micro-turbulence of 1, 2 and  $3 \text{ km s}^{-1}$ ; the enhancement in  $\alpha$ -elements of  $-0.4$ ,  $0.0$  and  $+0.4$ . The atomic data for the lines are from the compilation of Heiter et al. (2021) (see in APPENDIX A: Table A1). All the elements up to Zn have been computed by MyGIsFOS. For the heavy elements, the abundances have been derived as well by best-fit but the synthesis are based on Turbospectrum (Alvarez & Plez, 1998). The choice is related to the fact that the partition functions in Turbospectrum are more up-dated than the ones in SYNTHE. The use of SYNTHE to derive the abundances of the heavy elements would imply the use of older partition functions. On the one hand the SYNTHE grids are already available and we have invested considerable time to develop these grids (see e.g. Caffau et al., 2021). On the other hand the use of Turbospectrum to compute complete grids of synthetic spectra would be much more time consuming than with SYNTHE.

The abundances we derived are provided in Table 6. As usual, for each element X,  $A(X) = \log(N(X)/N(H)) + 12$ ,  $[X/H] = A(X) - A(X)_{\odot}$ , and  $[X/Fe] = [X/H] - [Fe/H]$ . The solar abundances,  $A(X)_{\odot}$ , here adopted are from Caffau et al. (2011) and Lodders et al. (2009) and are listed in Table 6. In all the figures, we show the LTE abundances, to be able to compare to the results from the literature.

We investigated in the literature for departure from local thermodynamical equilibrium and, when available, for each element we discussed how the NLTE corrections summarised in Table 7 was derived. The NLTE corrections, sometimes derived from a subsample of lines, were applied to the LTE abundances derived from the complete sample of lines. We verified that the LTE abundance from the subsample of lines was very close to the abundance derived from the complete sample of selected lines.

### 3.4 | Iron abundance

Fe I is usually the reference in the abundance determination because there is a fairly large numbers of lines in the stellar spectra of late type stars. Thanks to the good quality of the spectra, for both stars we could investigate with MyGIsFOS a large number of Fe I lines and derive an average  $A(\text{Fe})$  with a small line-to-line scatter of the order of 0.1 dex. The average Fe abundances we derived are reported in Table 6.

NLTE effects have been extensively studied in the literature (see e.g. Korn et al. 2003, Bergemann et al. 2012, Bergemann et al. 2012b, Mashonkina et al. 2016), in a large range of stellar parameters and over the entire spectrum from ultraviolet to infrared. It is at the lowest metallicities that NLTE corrections are usually the largest, while, for the same stellar parameters, these effects are usually small in the case of Fe II lines. Mashonkina et al. (2016) provided the NLTE corrections for

**TABLE 5** Parameters.

Star	$T_{\text{eff}}$ K	$\log g$ [cgs]	$\xi$ km s <sup>-1</sup>	[Fe/H]
TYC 622–742–1	4233 ± 100	0.71 ± 0.20	2.00 ± 0.20	-2.37 ± 0.10
TYC 1193–1918–1	4612 ± 100	1.67 ± 0.20	1.52 ± 0.20	-1.60 ± 0.10

**TABLE 6** Abundance ratio of the elements.

Element	Sun	TYC 622–742–1				TYC 1193–1918–1			
	A(X)	A(X) <sub>LTE</sub>	$\sigma(X)$	N(X)	A(X) <sub>NLTE</sub>	A(X) <sub>LTE</sub>	$\sigma(X)$	N(X)	
C	8.50	5.05	0.30	G-band		6.46	0.20	G-band	
N	7.86	6.90:	0.50	CN		6.84:	0.40	CN	
O I	8.76	7.25	0.13	2	7.25	7.75	0.14	1	7.75
Na I	6.30	3.83	0.01	2	3.83	4.52	0.10	5	4.52
Mg I	7.54	5.80	0.12	3	5.81	6.36	0.10	3	6.33
Al I	6.47					4.93	0.14	1	4.93
Si I	7.52	5.62	0.10	12	5.64	6.19	0.10	15	6.17
Ca I	6.33	4.35	0.10	21	4.49	5.17	0.08	28	5.22
Sc II	3.10	1.16	0.16	10		1.91	0.08	8	
Ti I	4.90	2.80	0.08	56		3.58	0.07	58	
Ti II	4.90	3.07	0.15	31	3.08	3.80	0.14	32	3.80
VI	4.00	1.56	0.11	15		2.34	0.08	18	
Cr I	5.64	3.16	0.10	17	3.46	4.00	0.08	17	4.21
Cr II	5.64	3.42	0.07	6		4.15	0.09	6	
Mn I	5.37	2.64	0.09	14	3.03	3.47	0.09	14	3.78
Fe I	7.52	5.15	0.10	254	5.25	5.92	0.10	298	5.98
Fe II	7.52	5.32	0.15	27	5.32	6.03	0.14	28	6.03
Co I	4.92	2.63	0.10	16	3.04	3.33	0.12	18	3.62
Ni I	6.23	3.85	0.12	52		4.60	0.13	58	
Cu I	4.21	1.29	0.08	3		2.08	0.12	4	
Zn I	4.62	2.20	0.16	1		3.08	0.03	2	
Sr II	2.92	0.70	0.16	1	0.80	1.25	0.14	1	1.25
Y II	2.21	-0.27	0.05	9		0.39	0.05	10	
Zr I	2.62	0.60	0.16	1		1.00	0.14	1	
Zr II	2.62	0.50	0.07	3		1.20	0.08	3	
Ba II	2.17	-0.08	0.02	3	-0.23	0.60	0.04	3	0.44
La II	1.14	-0.84	0.05	11		-0.34	0.04	14	
Ce II	1.61	-0.58	0.05	6		-0.03	0.07	7	
Pr II	0.76	-0.95	0.08	4		-0.62	0.06	3	
Nd II	1.45	-0.46	0.05	29		0.04	0.07	26	
Sm II	1.00	-0.78	0.04	9		-0.29	0.06	8	
Eu II	0.52	-1.00	0.16	1	-0.90	-0.50	0.14	1	-0.40

a large sample of the Fe I lines<sup>5</sup>. In this database we searched

for the lines used in our analysis. We entered the parameters of each star ( $T_{\text{eff}}$ ,  $\log g$  and metallicity) and derived the NLTE correction for 94 and 102 lines for TYC 622–742–1 and

<sup>5</sup><http://spectrum.inasan.ru/nLTE/>

TYC 1193–1918–1, respectively. The value for the NLTE correction of the Fe I we derive is: +0.10 dex for TYC 622–742–1 and +0.06 dex for the star TYC 1193–1918–1 (see Table 7). From these lines, we derived an average LTE  $A(\text{Fe})$  of 5.16 and 5.93, respectively, very close to the LTE Fe abundance derived from all the lines. We feel safe to apply these NLTE corrections to the  $[\text{Fe}/\text{H}]$  LTE abundances, and we obtain  $[\text{Fe}/\text{H}]$  of  $-2.27$  and  $-1.54$  for the two stars.

In the case of Fe II, by looking at the database [https://nlte.mpia.de/gui-siuAC\\_secE.php](https://nlte.mpia.de/gui-siuAC_secE.php) (Bergemann et al. 2012, Bergemann et al. 2012b), we see that the NLTE corrections provided are negligible in the case of our two stars. By applying the NLTE correction to our LTE analysis,  $A(\text{Fe})$  derived for Fe I and Fe II lines are in agreement ( $-2.27$  and  $-2.20$  for TYC 622–742–1;  $-1.54$  and  $-1.49$  for TYC 1193–1918–1), so we find a good ionisation equilibrium.

### 3.5 | Comparison samples

A goal of this investigation was to understand if these stars have peculiarities and the best way to do so is to compare the stars to literature investigations. We decided to compare these two stars to: (i) the sample by Gratton et al. (2000) composed by field stars, 17 of which are evolved stars, in the metallicity range  $-2 \leq [\text{Fe}/\text{H}] \leq -1$ ; (ii) the metal-poor sample of giant stars analysed by Cayrel et al. (2004), which consists of stars more metal-poor, but the extremely careful analysis is based on high-quality spectra and is a widely used reference sample; (iii) the stars presented in Fulbright (2000), that are more extended in metallicity and this sample contains some high-speed stars; (iv) two high-speed stars from Valentini et al. (2019); (v) the FORS high-speed stars sample investigated by Caffau et al. (2020a).

## 3.6 | Light elements

### 3.6.1 | Lithium

The Li doublet at 670.7 nm is not detectable: as expected in evolved stars, both stars already destroyed Li in their photosphere (see e.g. Salaris & Weiss, 2001).

### 3.6.2 | Carbon

The C abundance was derived from the G-band by line profile fitting, with  $\chi^2$  minimisation (see Bonifacio & Caffau, 2003). With the code SYNTHE (Kurucz, 2005), we computed synthetic spectra based on ATLAS 12 models (Kurucz, 2005) computed specifically for the two stars. The theoretical synthesis in the wavelength range of the band were computed by using the list of CH molecules provided by Masseron et al. (2014). The C abundances derived for the two stars are listed in Table 6.

In Fig. 3, the  $[\text{C}/\text{Fe}]$  ratios we derived are compared to literature results. Both stars have a low  $[\text{C}/\text{Fe}]$  ratio ( $[\text{C}/\text{Fe}]$  of  $-1.08$  and  $-0.44$ , respectively), and especially TYC 622–742–1, but, partially, this is expected in stars at these evolutionary stages. One can see from the figure that the low  $A(\text{C})$  is common in evolved stars. We are aware that this computation is sensitive to hydrodynamical effects, already investigated for unevolved stars by e.g. Gallagher et al. (2016). Although the stars here investigated are evolved, we do not have 3D models with such a low gravity, but negative 3D corrections could be expected.

We derived the isotopic ratio ( $^{12}\text{C}/^{13}\text{C} = 4.91_{-1.9}^{+6.5}$ ) only for TYC 1193–1918–1 from the two CH lines at 423.14 nm. The CH lines are too weak in TYC 622–742–1 to allow to derive the isotopic ratio.

### 3.6.3 | Nitrogen

Nitrogen abundances have been derived by fitting the weak CN band at around 418 nm. These weak lines lie in a crowded region, so the abundance determination is challenging. The procedure adopted was the same as for the C abundance determination, with the variance that in the spectral synthesis computation  $A(\text{C})$  was fixed at the values derived from the G-band. The N abundances we derived are reported in Table 6.  $A(\text{N})$  is very high for TYC 622–742–1 ( $[\text{N}/\text{Fe}] = 1.42$ ), and this could be related to the low C abundance for the fact that C has been converted in N. The effect is less dramatic for TYC 1193–1918–1 ( $[\text{N}/\text{Fe}] = +0.58$ ), but still visible by the enhancement in N.  $A(\text{N})$  determination is very uncertain overall for TYC 622–742–1 that is more metal-poor and we highlighted it in Table 6.

### 3.6.4 | Oxygen

Both forbidden [OI] lines are in the range of the Subaru spectra and they are both strong enough on these evolved stars to be useful for abundance determination. Unfortunately, the line at 630 nm falls in a range polluted by telluric absorptions, so depending on the radial velocity of each star and on the observing time, this line is or is not clear from telluric contamination. We could then analyse this line only for TYC 622–742–1. The O abundances derived, based on both [OI] lines for TYC 622–742–1 and only on the 636 nm line for TYC 1193–1918–1, are listed in Table 6. The forbidden oxygen lines form in conditions close to local thermodynamical equilibrium (see e.g. Sitnova et al., 2013). In Fig. 3, the  $[\text{O}/\text{Fe}]$  we derived for the two stars are compared to the analysis by Gratton et al. (2000).

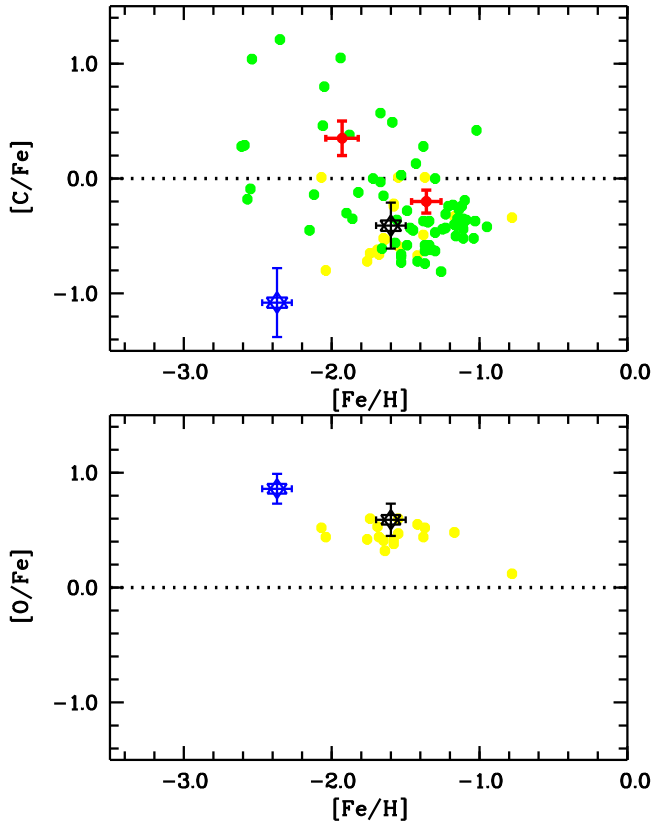


**FIGURE 3** Abundance ratios of the [C/Fe] (upper panel) and [O/Fe] (lower panel) as a function of [Fe/H]. The blue and black stars refer to the present study, TYC 622–742–1 and TYC 1193–1918–1, respectively, compared to two high-speed stars from Valentini et al. (2019, red dots), high-speed stars from Caffau et al. (2020a, green dots) and the evolved stars from Gratton et al. (2000, yellow dots) sample.

### 3.7 | $\alpha$ elements

#### 3.7.1 | Magnesium

To derive  $A(\text{Mg})$ , the lines at 470.2, 552.8 and 571.0 nm have been retained by MyGIsFOS for both stars. For the star TYC 622–742–1 we obtained  $[\text{Mg}/\text{Fe}] = 0.63 \pm 0.16$  dex and for the star TYC 1193–1918–1 we derived  $[\text{Mg}/\text{Fe}] = 0.42 \pm 0.14$  dex. In Table 6 the Mg abundances are listed.

In Alexeeva et al. (2018) a star with similar parameters (HD 122563) was investigated providing a negligible NLTE corrections for the two Mg I lines at 470.2 and 552.8 nm. We derived the NLTE corrections from Bergemann et al. (2017) by using the database<sup>6</sup>. For the lines employed by the MyGIsFOS analysis, we obtained a correction of 0.01 dex for TYC 622–742–1 and of  $-0.03$  dex for TYC 1193–1918–1 (see Table 7). By applying the NLTE corrections on Mg and Fe

abundances, we derived  $[\text{Mg}/\text{Fe}] = 0.54$  for TYC 622–742–1 and  $[\text{Mg}/\text{Fe}] = 0.33$  for TYC 1193–1918–1. In Fig. 4, the LTE  $[\text{Mg}/\text{Fe}]$  vs.  $[\text{Fe}/\text{H}]$  are compared to literature data.

#### 3.7.2 | Silicon

Several Si I features have been used (12 and 15 in the two stars, see Table 6) to derive the LTE Si abundance. Si I lines are sensitive to NLTE effects and the LTE silicon abundances are usually higher than the NLTE ones and these effects are more pronounced at low metallicity (see Bergemann et al., 2013). We derived the NLTE correction provided by Bergemann et al. (2013). We looked for the line studied with MyGIsFOS and present in the database and we obtained small NLTE corrections: a NLTE correction of  $+0.02$  dex for TYC 622–742–1 (see Table 7), from which we derive  $[\text{Si}/\text{Fe}] = 0.39$  and a NLTE correction of  $-0.02$  dex for TYC 1193–1918–1, which implies  $[\text{Si}/\text{Fe}] = 0.19$ . For both stars, the LTE Si abundance derived from the subsample of Si I lines for which a NLTE correction is available is just 0.02 dex higher.

#### 3.7.3 | Calcium

Several Ca I lines are available in the wavelength of the Subaru spectra. For the two stars 22 and 28 lines, respectively, are used for the abundance determination and they provide a very low line-to-line scatter (see Table 6). According to Spite et al. (2012), in the case of  $[\text{Ca}/\text{H}] \geq -2$  there is a negative NLTE correction: due to the NLTE effects the line wings weaken while the line core strength compared to the LTE case. For the stellar parameters of the two stars here analysed, the NLTE effects significantly affect the Ca I line profiles (see Mashonkina et al., 2016). We derived the NLTE correction for a subsample of the Ca I lines (from which we derived an LTE  $A(\text{Ca})$  0.03 and 0.02 dex higher than from the complete sample, respectively) here analysed from Mashonkina et al. (2016) (using the same method described in Sec. 3.4): 0.14 dex for TYC 622–742–1 and 0.05 dex for TYC 1193–1918–1 (see Table 7). These NLTE corrections provide for the  $[\text{Ca}/\text{Fe}]$  ratio the values 0.44 and 0.43, for the two stars respectively.

In Fig. 4, the LTE investigation of  $[\text{Ca}/\text{Fe}]$  vs.  $[\text{Fe}/\text{H}]$  is shown. In the figure one can see that few stars in the sample by Fulbright (2000) (pink dots) and in the sample by Caffau et al. (2020a) (green dots) have slightly lower  $[\text{Ca}/\text{Fe}]$ .

#### 3.7.4 | Titanium

Ti abundance was derived from neutral and single ionised lines for both stars. The  $[\text{Ti}/\text{Fe}]$  ratios when using Ti I lines are positive for both stars: 0.27 and 0.28, respectively. These values are consistent with the  $[\text{Ti}/\text{Fe}]$  ratios derived when the abundances are from the Ti II and Fe II lines: 0.36 and 0.39, respectively.

<sup>6</sup>[https://nlte.mpia.de/gui-siuAC\\_secE.php](https://nlte.mpia.de/gui-siuAC_secE.php)

The difference between Ti abundance when derived from neutral and ionised lines is non negligible (0.27 and 0.22 dex). These differences are also due to NLTE effects, which are strong in the case on Ti I lines (see Mashonkina et al., 2016). The NLTE effects for Ti I are more significant than for Fe I, which is directly reflected in the [Ti/Fe] ratio becoming larger in NLTE. By looking at the results by Mashonkina et al. (2016), we expect for both stars a NLTE correction of the order of 0.2 or 0.3 dex (see Table 7 ).

We investigated the NLTE corrections derived by Mashonkina et al. (2016) for the Ti I lines we used and present in the database, with the same procedure described in Sec. 3.4. For the selected lines we derive a NLTE correction for Ti I of +0.37 dex for TYC 622–742–1 and 0.14 dex for TYC 1193–1918–1. The lines with a NLTE correction available provide an LTE  $A(\text{Ti})$  0.01 and 0.03 dex higher than the abundance derived from the complete sample of Ti I lines, respectively for the two stars. By applying this NLTE correction, we derived for the [Ti/Fe] ratios 0.54 and 0.36 for the two stars, respectively. By looking at Figure 1 by Mashonkina et al. (2016) we think that, due to the limited number among the Ti I lines we used that are present in the investigation by Mashonkina et al. (2016), the NLTE correction for TYC 622–742–1 should be smaller, in the range 0.2–0.3 dex. In the case of Ti II we derived small NLTE corrections: 0.01 dex for TYC 622–742–1 and 0.00 dex for TYC 1193–1918–1, which provides [Ti/Fe] of 0.37 and 0.39 for the two stars (also in this case for  $A(\text{Fe})$  we used is from Fe II lines). The Ti abundance derived from the Ti II lines with NLTE correction is the same than when derived from the complete sample of lines.

### 3.7.5 | Summary $\alpha$ -elements

All the  $\alpha$ -elements we could derive (Mg, Si, Ca and Ti) are enhanced in the two stars, as expected in metal-poor stars (see Spite et al., 2012). In Fig. 4 our LTE results are compared to the literature data. The ratios of abundances of the  $\alpha$  elements are in very good agreement with the two high-speed stars from Valentini et al. (2019, see red dots in Fig. 4 ), the high-speed stars from Caffau et al. (2020a, green dots in Fig. 4 ), the evolved stars from the sample by Ishigaki et al. (2012, light blue dots in Fig. 4 ) and the evolved stars from Fulbright (2000, pink dots in Fig. 4 ).

## 3.8 | Odd-Z elements

### 3.8.1 | Sodium

Several Na I lines (498.2, 568.2, 568.8, 588.9, 589.6 and 616.0 nm) have been investigated to derive  $A(\text{Na})$  for the more metal-rich star TYC 1193–1918–1, and the line-to-line scatter we derived is small. The D1 and D2 lines provide abundances which are consistent with the values derived from the other

weak lines; this fact could be explain by looking at Figure 2 by Takeda et al. (2003), an investigation on NLTE effects (on all the lines we investigated, except the line at 498.2 nm) where they deduce that NLTE effects are strong for saturated lines and become insignificant with decreasing or increasing the strength of the lines. For TYC 622–742–1 only the two weak lines at 568 nm are used to derive the Na abundance. In Fig. 5 the abundances derived for the two stars are compared to literature analysis.

### 3.8.2 | Aluminium

Only for TYC 1193–1918–1 we could derive Al abundance, from the feature at 669.6 nm. Looking at the study by Nordlander & Lind (2017), we deduce that for the parameters of this star, the NLTE effects for aluminium are small. In Fig. 5 the [Al/Fe] ratio derived for TYC 1193–1918–1 is compared to the results by Fulbright (2000).

## 3.9 | Iron peak elements

### 3.9.1 | Scandium

We could derive  $A(\text{Sc})$  from a sample of ionised lines, that provide a small line-to-line scatter (see Table 6 ). The [Sc/Fe] ratios, when using the Fe abundance from ionised lines, are of 0.25 and 0.30 dex for TYC 622–742–1 and TYC 1193–1918–1, respectively. In Fig. 6 our results are compared to the ones by Ishigaki et al. (2012).

### 3.9.2 | Vanadium

For the abundance determination of V, a quite large sample of line has been used for both stars (see Table 7 ) that provide a small line-to-line scatter. The [V/Fe] ratios derived for the two stars are close to zero (see Fig. 6 ).

### 3.9.3 | Chromium

For the Cr abundance determination we could rely on both neutral and single ionised lines. For both stars the ionisation balance is not good and the Cr abundances derived from neutral lines are smaller for both stars, by 0.28 and 0.15 dex, respectively. This discrepancy is related to NLTE effects (see Bergemann et al., 2010).

We determine the NLTE corrections for our stars using the database by Bergemann et al. (2010), looking at all the lines used by MyGIsFOS in the analysis. We derived a NLTE correction of 0.30 and 0.21 dex for the two stars (see Table 7 ). We then derived  $[\text{Cr I}/\text{Fe}] = 0.09$  dex for TYC 622–742–1 and  $[\text{Cr I}/\text{Fe}] = 0.11$  dex for TYC 1193–1918–1. These values have to be compared to the LTE [Cr/Fe] ratio by taking into account the abundances derived from ionised lines, and we

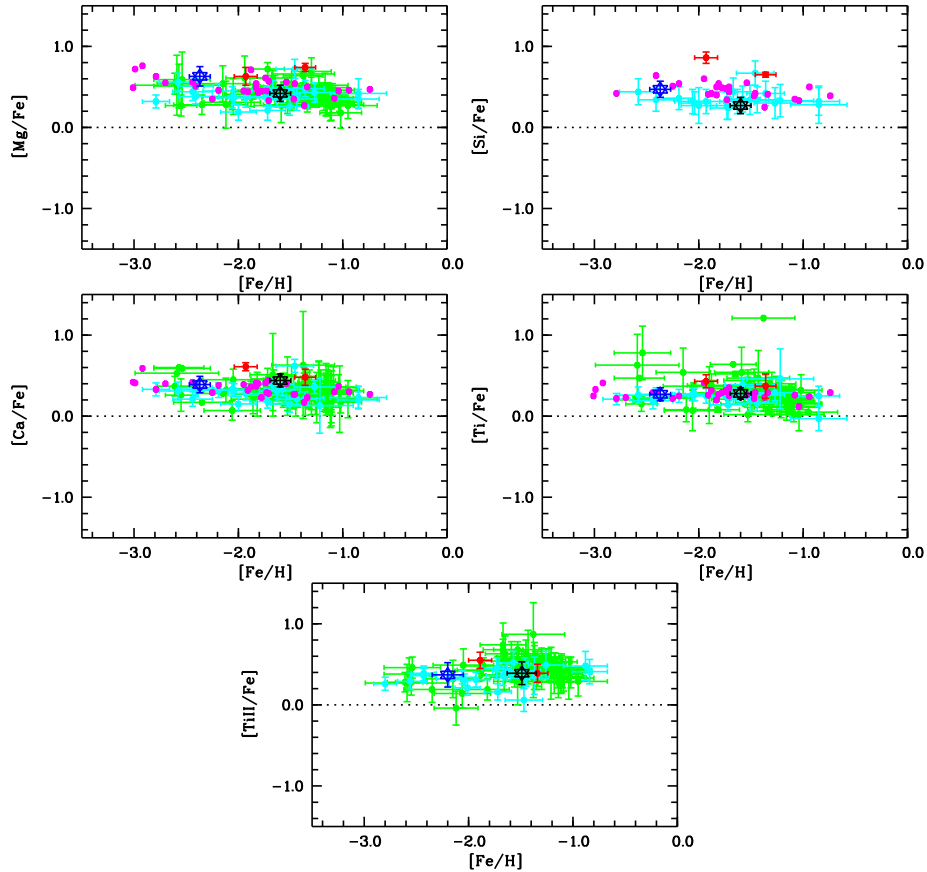


**FIGURE 4** Abundance ratios of the  $\alpha$  elements as a function of  $[\text{Fe}/\text{H}]$ . The blue and black star refer to the present study, TYC 622–742–1 and TYC 1193–1918–1, respectively, compared to two high-speed stars from Valentini et al. (2019, red dots), high-speed stars from Caffau et al. (2020a, green dots), the evolved stars from Ishigaki et al. (2012, light blue dots) and from Fulbright (2000, pink dots) sample.

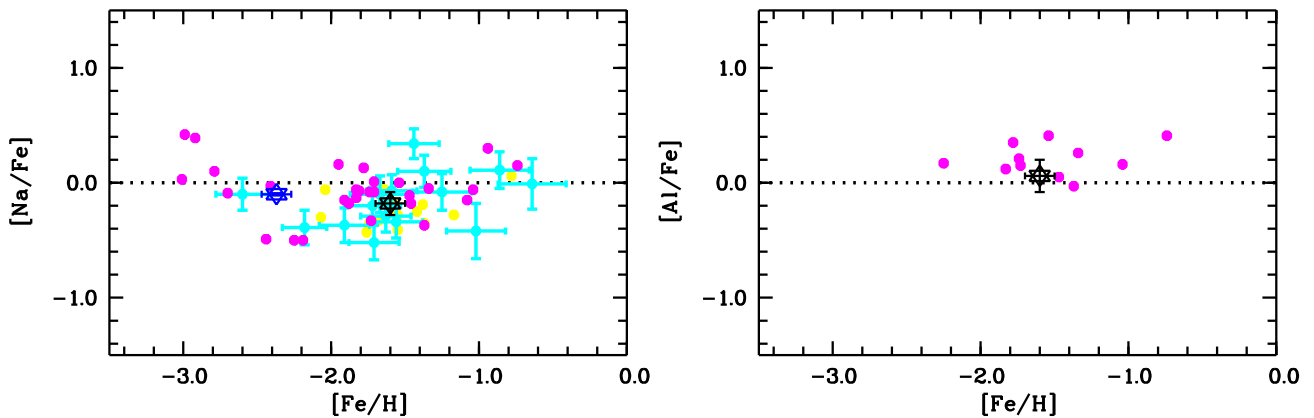


**FIGURE 5** Abundance ratios of the odd-Z elements as a function of  $[\text{Fe}/\text{H}]$ . The blue and black star refer to the present study, TYC 622–742–1 and TYC 1193–1918–1, respectively, compared to the evolved stars from Gratton et al. (2000, yellow dots), from Ishigaki et al. (2013, light blue dots) and from Fulbright (2000, pink dots) sample.

obtain:  $[\text{Cr}/\text{Fe}]$  of  $-0.03$  and  $0.00$ , for the two stars, in excellent agreement with the ratio from neutral lines once NLTE effects

are taken into account. The LTE  $[\text{Cr}/\text{Fe}]$  ratios we derived for both stars are shown in Fig. 6 .

### 3.9.4 | Manganese

Mn abundance was derived for the two stars from 14 features. Figure 6 shows how our two stars show slightly low Mn abundances, with [Mn/Fe] ratios of the order of  $-0.3$  dex, but fully compatible with the stars of other samples.

The LTE Mn abundances are systematically lower than NLTE abundances and the lower the metallicity, the larger the difference between NLTE and LTE. Bergemann & Gehren (2008) provided a NLTE corrections for Mn and we searched for the lines used in the MyGIsFOS analysis and derived a NLTE correction of 0.39 dex for TYC 622–742–1 and 0.31 dex for TYC 1193–1918–1 (see Table 7). If we take into account the NLTE corrections, we derive for the [Mn/Fe] ratios  $-0.07$  for TYC 622–742–1 and  $-0.05$  dex for TYC 1193–1918–1.

### 3.9.5 | Cobalt

Co abundance is based on 16 and 18 Co I lines, respectively for the two stars (see Table 6), that provide a low line-to-line scatter. The [Co/Fe] ratio is close to zero (0.08 and 0.01, respectively for the two stars, see Fig. 6). Bergemann et al. (2010) provide the NLTE correction for Co I. We searched for the lines analysed in MyGIsFOS and we obtain a NLTE correction of 0.41 dex for TYC 622–742–1, which provide [Co/Fe]=0.39 dex, and +0.32 dex for TYC 1193–1918–1, providing [Co/Fe]=0.27 (see Table 7).

### 3.9.6 | Nickel

A large sample of Ni I lines (55) are used to derive A(Ni). For both stars the line-to-line scatter is small (see Table 6) and the [Ni/Fe] is close to zero. In Fig. 6, [Ni/Fe] ratios are compared to literature values. To our knowledge no NLTE investigation exists on this element.

### 3.9.7 | Copper

Three Cu I lines are investigated at 510.5, 570.0 and 578.2 nm. For the star TYC 622–742–1 we also analysed the line at 521.8 nm. The copper over iron ratio is very consistent in the two stars of the sample:  $\langle [\text{Cu}/\text{Fe}] \rangle = -0.54 \pm 0.01$  dex. These values are in good agreement with the analysis by Ishigaki et al. (2013) (see Fig. 6). The NLTE effects, investigated by Andrievsky et al. (2018), are large for the lines here analysed. They get smaller as the metallicity increases. The NLTE effect would increase the Cu abundance and is of the order of  $\sim 0.5$  dex (see Table 7) for the more metal-rich star here analysed, and even larger for the other star (see Andrievsky et al., 2018). A NLTE correction of the order of 0.5 dex would bring the [Cu/Fe] ratio close to zero.

### 3.9.8 | Zinc

The Zn abundance was derived from the 481.1 nm line for TYC 622–742–1 and for the star TYC 1193–1918–1 we used the two Zn I lines at 481.1 and 472.2 nm lines. We derived [Zn/Fe] ratios close to zero ( $-0.04$  and  $0.06$  for the two stars). In Fig. 6 the [Zn/Fe] ratios we derived are compared to literature results.

## 3.10 | Neutron capture elements

For the heavy elements we fitted the line profile of the lines. We computed the synthetic spectra with Turbospectrum (Alvarez & Plez, 1998) by using ATLAS 12 models computed with the parameters derived for each star. Hyperfine splitting and solar mix isotopic ratios have been used for the computation of the abundances.

As one can see from Fig. 6, the stars are coherent with the results from the literature in the heavy elements. Both stars shows a low [Y/Fe] ratio and an enhancement in Eu, as several stars in the sample by Ishigaki et al. (2013) and Fulbright (2000). TYC 622–742–1 shows a slight enhancement also in Zr, Pr, Nd, Sm.

### 3.10.1 | Strontium

The Sr II line at 421.6 nm is employed to derive the Sr abundance. The [Sr/Fe] ratios in the two stars are both slightly negative:  $-0.05$  and  $-0.18$  for TYC 622–742–1 and TYC 1193–1918–1, respectively. In Fig. 7 the [Sr/Fe] ratios we derived for the two stars are compared to literature results. Andrievsky et al. (2011) analysed the NLTE effects in a sample of very and extremely metal-poor stars. For the star TYC 622–742–1, the NLTE correction on the Sr line used should be of the order of 0.1 dex; the other star is too metal-rich to fit in this investigation.

### 3.10.2 | Yttrium

The Y abundance has been derived by analysing 9 and 10 Y II lines for the two stars, respectively. We derive [Y/Fe] very close for the two stars ( $-0.31$  and  $-0.33$ , respectively, when using A(Fe) from ionised lines). In Fig. 7 our results are compared to literature values and we see a close coherence.

### 3.10.3 | Zirconium

For the determination of A(Zr) both Zr I (473.9 nm) and Zr II (420.8, 461.3 and 511.2 nm) lines have been investigated. For both stars A(Zr) derived from neutral and ionised lines are in agreement within the uncertainties (see Table 6). The star TYC 622–742–1 has a high value of [Zr/Fe] when the ratio is derived from Zr I and Fe I lines, while this ratio is close to zero

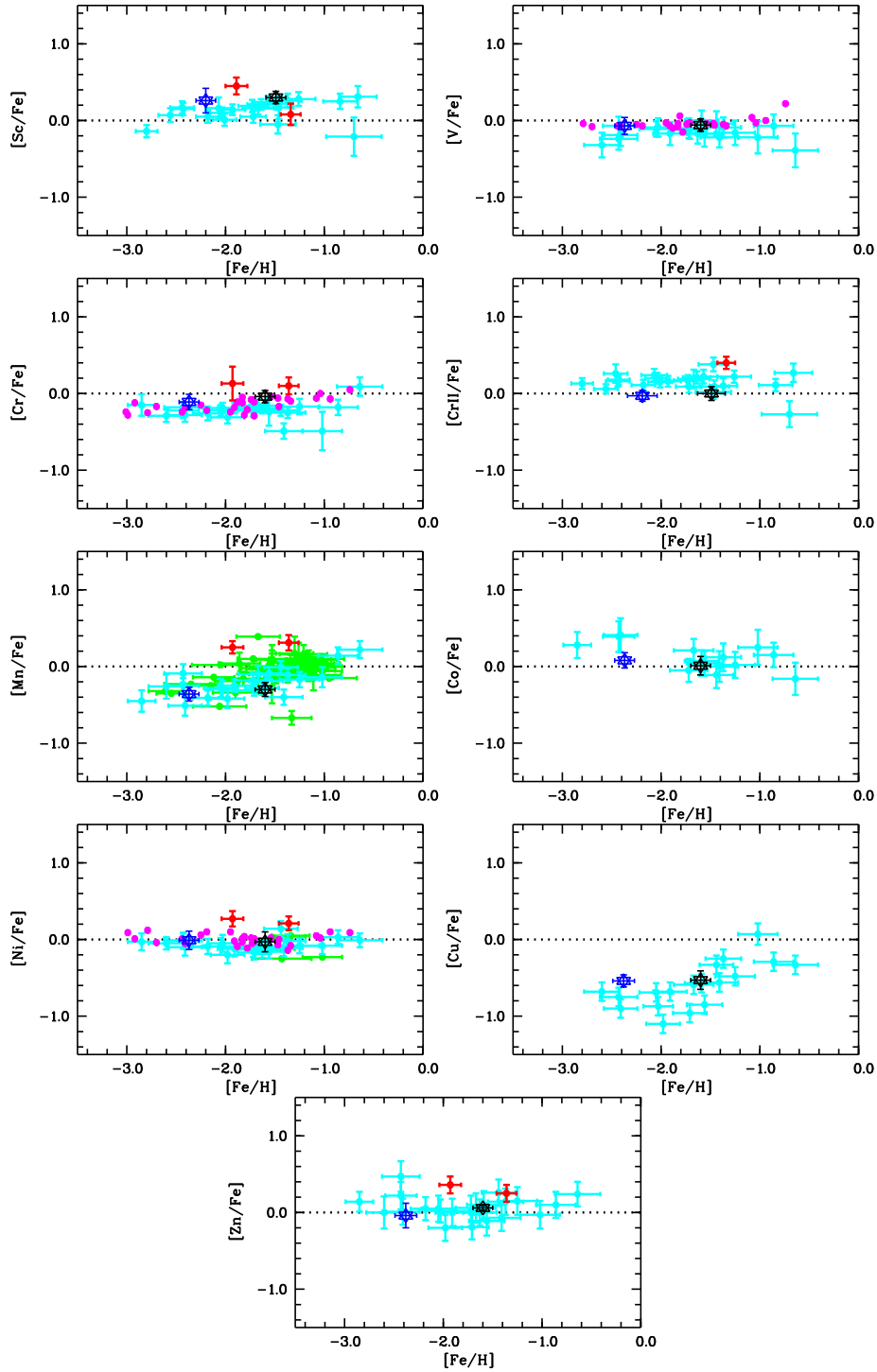


**FIGURE 6** Abundance ratios of iron peak elements as a function of  $[\text{Fe}/\text{H}]$ . The blue and black star refer to the present study, TYC 622–742–1 and TYC 1193–1918–1, respectively, compared to two high-speed stars from Valentini et al. (2019, red dots), high-speed stars Caffau et al. (2020a, green dots) and the evolved stars from Ishigaki et al. (2013, light blue dots) and from Fulbright (2000, pink dots) sample.

(0.05 dex) when the abundances are from ionised lines, Zr II and Fe II. For the star TYC 1193–1918–1, the values of  $[\text{Zr}/\text{Fe}]$  are in good agreement when the abundances are derived from

neutral Zr I and Fe I lines or ionised Zr II and Fe II lines. In Fig. 7  $[\text{Zr}/\text{Fe}]$  from ionised lines is compared to literature values.

### 3.10.4 | Barium

To derive  $A(\text{Ba})$  three Ba II lines have been selected for each star. For TYC 622–742–1 the selected lines (at 493.4, 585.3 and 649.6 nm) provided an LTE abundance of  $A(\text{Ba}) = -0.08 \pm 0.02$  (see Table 6), with  $[\text{Ba}/\text{Fe}] = -0.05$ , when  $A(\text{Fe})$  is from Fe II lines. For TYC 1193–1918–1, in LTE we derived  $A(\text{Ba}) = 0.60 \pm 0.04$  (see Table 6,  $[\text{Ba}/\text{Fe}] = -0.08$ ) by investigating three Ba II lines (at 585.3, 614.1 and 649.6 nm). Korotin et al. (2015) investigated the NLTE corrections for a sample of Ba II lines. For TYC 622–742–1 two lines are in the sample investigated by Korotin et al. (2015) (from which we derive an LTE abundance  $A(\text{Ba}) = -0.07$ ) and for them we derived a NLTE correction of the order of  $-0.15$ , which, applied to the LTE abundance derived from all lines we derive  $A(\text{Ba}) = -0.22$  and  $[\text{Ba}/\text{Fe}] = -0.20$  dex. For TYC 1193–1918–1 the three lines are in the set investigated by Korotin et al. (2015) and we derive a NLTE correction of about  $-0.16$ , providing:  $A(\text{Ba}) = 0.44$  and  $[\text{Ba}/\text{Fe}] = -0.24$  dex. In Fig. 7,  $[\text{Ba}/\text{Fe}]$  is compared to results from the literature.

### 3.10.5 | Lanthanum

A considerable sample of La II lines (15 and 14, respectively) has been investigated to derive  $A(\text{La})$  of  $-0.84 \pm 0.05$  and  $-0.34 \pm 0.04$  for the two stars, respectively (see Table 6). By using the Fe abundance from the ionised lines, we derive  $[\text{La}/\text{Fe}]$  ratios of 0.19 and 0.01, respectively (see Fig. 7).

### 3.10.6 | Cerium

Seven Ce II features are used to derive  $A(\text{Ce})$  of  $-0.58 \pm 0.05$  and  $-0.03 \pm 0.07$  for the two stars (see Table 6), which provides  $[\text{Ce}/\text{Fe}]$  of  $-0.02$  and  $-0.15$ , respectively, when using the Fe abundance derived from ionised lines.

### 3.10.7 | Praseodymium

The TYC 622–742–1 star presents a high value of Pr ( $A(\text{Pr}) = -0.95 \pm 0.08$  and  $[\text{Pr}/\text{Fe}] = 0.46$ ) derived from a sample of four Pr II lines. For TYC 1193–1918–1, three lines analysed provide  $A(\text{Pr}) = -0.62 \pm 0.06$  and  $[\text{Pr}/\text{Fe}] = 0.11$ . For the  $[\text{Pr}/\text{Fe}]$  ratios  $A(\text{Fe})$  is from ionised lines. The Pr abundances are listed in Table 6 and shown in Fig. 7.

### 3.10.8 | Neodymium

Nd is well represented in the Subaru spectra here analysed: a sample of 29 and 26 lines have been analysed for TYC 622–742–1 and TYC 1193–1918–1, respectively, providing  $A(\text{Nd})$  of  $-0.46 \pm 0.05$  and  $0.04 \pm 0.07$  for the two stars (see Table 6). We could then derive  $[\text{Nd}/\text{Fe}]$  ratios of 0.26 and  $-0.08$  dex (see Fig. 7) for the two stars, with  $A(\text{Fe})$  from Fe II lines.

### 3.10.9 | Samarium

To derive  $A(\text{Sm})$  eleven and ten Sm II features have been analysed, providing  $A(\text{Sm})$  of  $-0.78 \pm 0.04$  and  $-0.29 \pm 0.06$  and  $[\text{Sm}/\text{Fe}]$  of 0.39 and 0.20 dex, respectively. In Table 6  $A(\text{Sm})$  are reported.

### 3.10.10 | Europium

Just the Eu II line at 664.5 nm allowed us to derive  $A(\text{Eu})$  of  $-1.0$  and  $-0.5$  (see Table 6), respectively. For both stars we derive a positive  $[\text{Eu}/\text{Fe}]$  ratio (0.65 and 0.47 for the two stars). Both stars, but particularly TYC 622–742–1, show a high value of Eu (see Fig. 7).

## 3.11 | Uncertainties

When several lines are available in the abundance determination, we adopted the line-to-line scatter as uncertainty on the abundance determination, and the value is listed in Table 6. For the elements whose abundances are based on one single lines we took the highest line-to-line scatter, which is 0.16 dex for TYC 622–742–1 and 0.14 dex for TYC 1193–1918–1.

Our uncertainties on the stellar parameters are:  $\Delta T = 100$  K,  $\Delta \log g = 0.10$  dex and  $\Delta \xi = 0.20$  km s<sup>-1</sup>. A change in the stellar parameters brings a change in the abundance derived for the star. We then run MyGIsFOS by changing the stellar parameters with these uncertainties, to quantify the uncertainties in the abundances due to the uncertainties in the stellar parameters, and we derived the changes in the abundances listed in Table 8. The largest uncertainties in the abundance determination arise usually from the uncertainty in the temperature of the stars.

## 4 | DISCUSSION

### 4.1 | Parallax zero-point

To derive the stellar parameters, we applied the zero-point as described by Lindegren et al. (2021). In the case we have not applied the zero-point the star TYC 1193–1918–1 would have been barely affected, while for the star TYC 622–742–1 small changes, anyway within the uncertainties, would have affected the stellar parameters. We would have derived: (i) a  $T_{\text{eff}}$  hotter by about 30 K for TYC 622–742–1 and just few K for TYC 1193–1918–1; (ii) a  $\log g$  smaller by more than 0.1 dex for TYC 622–742–1 and by 0.05 dex for TYC 1193–1918–1.

### 4.2 | Kinematics

The stellar orbits, integrated 10 Gyr backwards, are presented in Fig. 8 (blue and orange for TYC 622–742–1 and

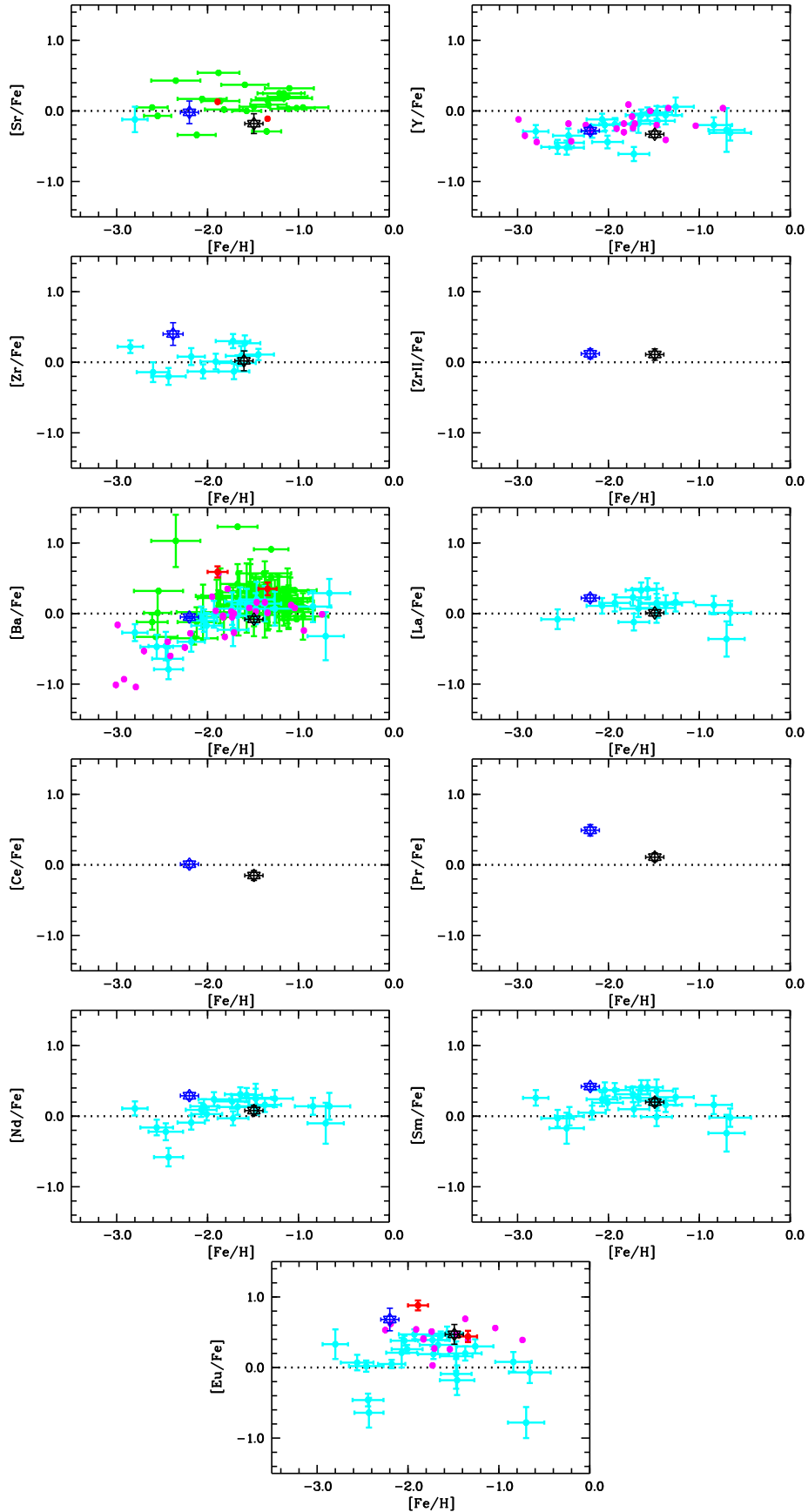


FIGURE 7 Same as Fig. 6 for neutron capture elements.

**TABLE 7** NLTE corrections applied to the two stars in the sample.

element	TYC 622–742–1 NLTE correction	TYC 1193–1918–1 NLTE correction	reference
O I	0.00	0.00	Sitnova et al. (2013)
Na I	0.00	0.00	Takeda et al. (2003)
Mg I	0.01	–0.03	Bergemann et al. (2017)
Al I		0.00	Nordlander & Lind (2017)
Si I	0.02	–0.02	Bergemann et al. (2013)
Ca I	0.14	0.05	Mashonkina et al. (2016)
Ti I	0.37	0.14	Mashonkina et al. (2016)
Ti II	0.01	0.00	Mashonkina et al. (2016)
Cr I	0.30	0.21	Bergemann et al. (2010)
Mn I	0.39	0.31	Bergemann & Gehren (2008)
Fe I	0.10	0.06	Mashonkina et al. (2016)
Fe II	0.00	0.00	Mashonkina et al. (2016)
Co I	0.41	0.32	Bergemann et al. (2010)
Cu I	0.50	0.50	Andrievsky et al. (2018)
Sr II	0.10		Andrievsky et al. (2011)
Ba II	–0.15	–0.16	Korotin et al. (2015)

TYC 1193–1918–1, respectively). Both stars present retrograde, eccentric orbits ( $e=0.32$  and  $0.70$ , respectively for TYC 622–742–1 and TYC 1193–1918–1). Their orbital and kinematical parameters are typical of halo stars. None of them seem to belong to the Gaia-Sausage-Enceladus (GSE) structure (Belokurov et al., 2018; Di Matteo et al., 2019; Haywood et al., 2018; Helmi et al., 2018). Figure 9 presents the position of the two stars (blue triangle and orange square for TYC 622–742–1 and TYC 1193–1918–1, respectively) in planes used to isolate GSE, employing Galactocentric cylindrical velocities ( $V_T$ ,  $V_R$ ,  $V_Z$ , top panels), the vertical component of the angular momentum ( $L_Z$ , bottom panels), the orbital energy ( $E$ , bottom-right panel), and the radial action (its square root  $\sqrt{J_R}$ , bottom-left panel). As a reference sample, stars of the “good parallax” sub-sample analysed in Bonifacio et al. (2021) are also plotted in gray scale. The red-shaded area in the bottom-left panel corresponds to the criteria defined in Feuillet et al. (2020) to select GSE stars, namely  $-500 \text{ kpc km s}^{-1} < L_Z < 500 \text{ kpc km s}^{-1}$  and  $30 < \sqrt{J_R} < 50$ . Stars belonging to this area are then presented as red filled circles in the other panels. TYC 622–742–1 has  $V_T$  and  $L_Z$  relatively similar to GSE stars, but a significantly lower value of  $\sqrt{J_R}$ .

### 4.3 | Abundances

The stars mainly show a typical chemical pattern of metal-poor evolved stars, as also highlighted by the comparison with the literature samples.

The stars with retrograde motion studied by Matsuno et al. (2019) show decreasing trend of  $[\alpha/\text{Fe}]$  with increasing metallicity. The decrease appears at about  $[\text{Fe}/\text{H}] > -2$ . The two stars here analysed differ in  $[\text{Fe}/\text{H}]$ , with TYC 622–742–1 having  $[\text{Fe}/\text{H}] < -2$  and TYC 1193–1918–1  $[\text{Fe}/\text{H}] > -2$ . From Fig. 4 and Table 6 one can see that the most metal-rich star (TYC 1193–1918–1) has lower  $[\text{Mg}/\text{Fe}]$  and  $[\text{Si}/\text{Fe}]$  than the most metal-poor star (TYC 622–742–1) following exactly the trend suggested by Matsuno et al. (2019). This trend is also found for GSE stars, but it is more significant in retrograde stars.

TYC 1193–1918–1 is probably an RGB star (see Fig. 2). TYC 622–742–1 could also be an RGB star, but the AGB solution is also reasonable from its photometry and parallax and we are more in favour of this latter possibility due to its low C and high N abundances. We recall the large uncertainty in the A(N) determination, but still the derived values are consistent with the literature results. The C abundance is low in both stars, while A(N) is high, but this can be expected in evolved stars, when part of the carbon has been converted into nitrogen and due to some ill understood mechanism, occurring after the RGB bump often dubbed as extra mixing or non-standard mixing (see e.g. Charbonnel et al., 2020, and references therein), it is brought to the stellar surface. Anyway, in TYC 622–742–1 the effect seems quite extreme (see Fig. 3). The  $[(\text{C}+\text{N})/\text{Fe}]$ , defined as  $\log((\text{C} + \text{N})/\text{Fe}) - \log((\text{C} + \text{N})/\text{Fe})_{\odot}$ , is close to 0 for TYC 1193–1918–1, but it is +0.7 dex for TYC 622–742–1.

According to Placco et al. (2014), a star with the surface gravity of TYC 622–742–1, with a  $\log g$  increased by 0.5 dex

**TABLE 8** Sensitivity of abundances on atmospheric parameters

Element	TYC 622–742–1			TYC 1193–1918–1		
	$\Delta T_{\text{eff}} = \pm 100$ K	$\Delta \log g = \pm 0.2$	$\Delta \xi = \pm 0.2$ $\text{km s}^{-1}$	$\Delta T_{\text{eff}} = \pm 100$ K	$\Delta \log g = \pm 0.2$	$\Delta \xi = \pm 0.2$ $\text{km s}^{-1}$
O I	-0.03/+0.02	-0.13/+0.12	+0.00/+0.00	-0.01/ + 0.02	-0.11/ + 0.13	+0.00/ + 0.01
Na I	-0.10/+0.04	+0.01/-0.02	+0.00/+0.00	-0.09/ + 0.08	+0.02/ - 0.04	+0.02/ - 0.02
Mg I	-0.08/+0.08	+0.02/-0.03	+0.03/-0.01	-0.09/ + 0.09	+0.03/ - 0.03	+0.06/ - 0.05
Al I				-0.09/ + 0.05	+0.00/ - 0.01	+0.00/ + 0.00
Si I	-0.02/+0.05	-0.02/+0.01	+0.00/+0.00	+0.00/ + 0.04	-0.02/ + 0.03	+0.01/ + 0.00
Ca I	-0.09/+0.10	+0.02/-0.02	+0.04/-0.02	-0.11/ + 0.10	+0.01/ - 0.01	+0.06/ - 0.06
Sc II	+0.02/-0.02	-0.11/+0.11	+0.04/-0.02	+0.02/ - 0.01	-0.12/ + 0.12	+0.05/ - 0.04
Ti I	-0.20/+0.16	+0.02/-0.01	+0.03/-0.01	-0.15/ + 0.15	+0.02/ - 0.01	+0.05/ - 0.03
Ti II	+0.02/-0.01	-0.07/+0.08	+0.06/-0.04	-0.01/ + 0.00	-0.10/ + 0.10	+0.08/ - 0.09
V I	-0.18/+0.16	+0.01/-0.02	+0.00/+0.00	-0.19/ + 0.16	+0.01/ - 0.01	+0.00/ - 0.01
Cr I	-0.16/+0.14	+0.02/-0.02	+0.03/-0.03	-0.13/ + 0.12	+0.01/ - 0.01	+0.04/ - 0.04
Cr II	+0.06/-0.04	-0.07/+0.09	+0.01/+0.00	+0.02/ - 0.01	-0.08/ + 0.09	+0.03/ - 0.02
Mn I	-0.14/+0.14	+0.02/-0.03	+0.01/-0.01	-0.14/ + 0.11	+0.01/ - 0.01	+0.02/ - 0.02
Fe I	-0.12/+0.12	+0.02/-0.01	+0.05/-0.04	-0.11/ + 0.11	+0.00/ + 0.00	+0.06/ - 0.06
Fe II	+0.10/-0.06	-0.09/+0.11	+0.05/-0.02	+0.09/ - 0.06	-0.12/ + 0.12	+0.06/ - 0.07
Co I	-0.13/+0.15	+0.00/-0.01	+0.00/+0.00	-0.14/ + 0.13	+0.00/ + 0.01	+0.01/ + 0.00
Ni I	-0.10/+0.09	+0.00/-0.01	+0.01/-0.02	-0.09/ + 0.09	-0.01/ + 0.01	+0.03/ - 0.03
Cu I	-0.12/+0.13	+0.02/-0.01	+0.00/+0.00	-0.14/ + 0.12	+0.00/ - 0.01	+0.00/ - 0.01
Zn I	+0.05/-0.03	-0.06/+0.05	+0.03/-0.02	+0.04/ - 0.01	-0.06/ + 0.07	+0.08/ - 0.06
Sr II	-0.10/+0.09	+0.00/-0.01	+0.15/-0.12	-0.13/ + 0.12	-0.01/ + 0.03	+0.16/ - 0.13
Y II	-0.05/+0.05	-0.07/+0.06	+0.04/-0.03	-0.03/ + 0.03	-0.09/ + 0.09	+0.05/ - 0.05
Zr I	-0.21/+0.11	+0.00/+0.00	+0.00/+0.00	-0.13/ + 0.12	-0.01/ + 0.01	+0.00/ + 0.00
Zr II	+0.02/-0.01	-0.08/+0.11	+0.04/-0.02	+0.01/ + 0.02	-0.11/ + 0.13	+0.04/ - 0.05
Ba II	-0.04/+0.06	-0.09/+0.10	+0.21/-0.14	-0.05/ + 0.05	-0.11/ + 0.11	+0.28/ - 0.23
La II	-0.04/+0.04	-0.09/+0.10	+0.01/-0.01	-0.04/ + 0.05	-0.08/ + 0.10	+0.01/ - 0.01
Ce II	-0.08/+0.07	-0.07/+0.07	+0.00/+0.00	-0.07/ + 0.05	-0.07/ + 0.09	+0.03/ - 0.01
Pr II	-0.04/+0.05	-0.10/+0.10	+0.00/+0.00	-0.04/ + 0.04	-0.09/ + 0.12	+0.00/ + 0.00
Nd II	-0.07/+0.06	-0.07/+0.09	+0.02/+0.00	-0.04/ + 0.04	-0.10/ + 0.08	+0.00/ - 0.01
Sm II	-0.06/+0.05	-0.13/+0.11	+0.03/-0.02	-0.06/ + 0.05	-0.10/ + 0.10	+0.02/ - 0.02
Eu II	+0.03/-0.03	-0.12/+0.16	+0.00/+0.00	-0.02/ + 0.00	-0.09/ + 0.12	+0.01/ + 0.00

as they suggest, had the initial carbon of about 0.7 dex higher. So the star was C-poor also on the main sequence, with  $[C/Fe]$  of about  $-0.4$  dex. Looking at Figure 1 in Placco et al. (2014), the star TYC 622–742–1 was C-poor on the main sequence and also N-rich by about the same amount at the present evolutionary state. In Fig. 10 the  $[N/Fe]$  ratio is plotted as a function of the  $[C/Fe]$  ratio. The star TYC 1193–1918–1 shows abundance ratios similar to many stars in the two comparison sample, while TYC 622–742–1 stands out, with an extremely low  $[C/Fe]$  ratio joint to a high  $[N/Fe]$ .

The high  $[N/Fe]$  and low  $[C/Fe]$  ratios are surely an evolution effect. From Fig. 11, one can see that the star TYC 1193–1918–1 is perfectly coherent with the comparison sample by

Gratton et al. (2000, yellow dots) which is close in metallicity. Instead, the star TYC 622–742–1, compared to the sample by Spite et al. (2005, green dots) seems a bit on the edge (see Fig. 11).

We queried the SAGA database (Suda et al., 2008) to select the metal-poor stars with low  $[C/Fe]$  ( $[C/Fe] < -0.8$ ). We removed the stars from Li et al. (2013), whose C abundance is derived from infrared CO lines. We end up with a sample of: nine stars from Hansen et al. (2018) who derived A(C) from the G-band (2MASS J02412152-1825376, J14164084-2422000, J15260106-0911388, J17094926-6239285, J19161821-5544454, J20093393-3410273, J21162185-0213420, J21262525-2144243, J21513595-0543398); two stars from Aoki & Honda (2008): HD 29574 observed also

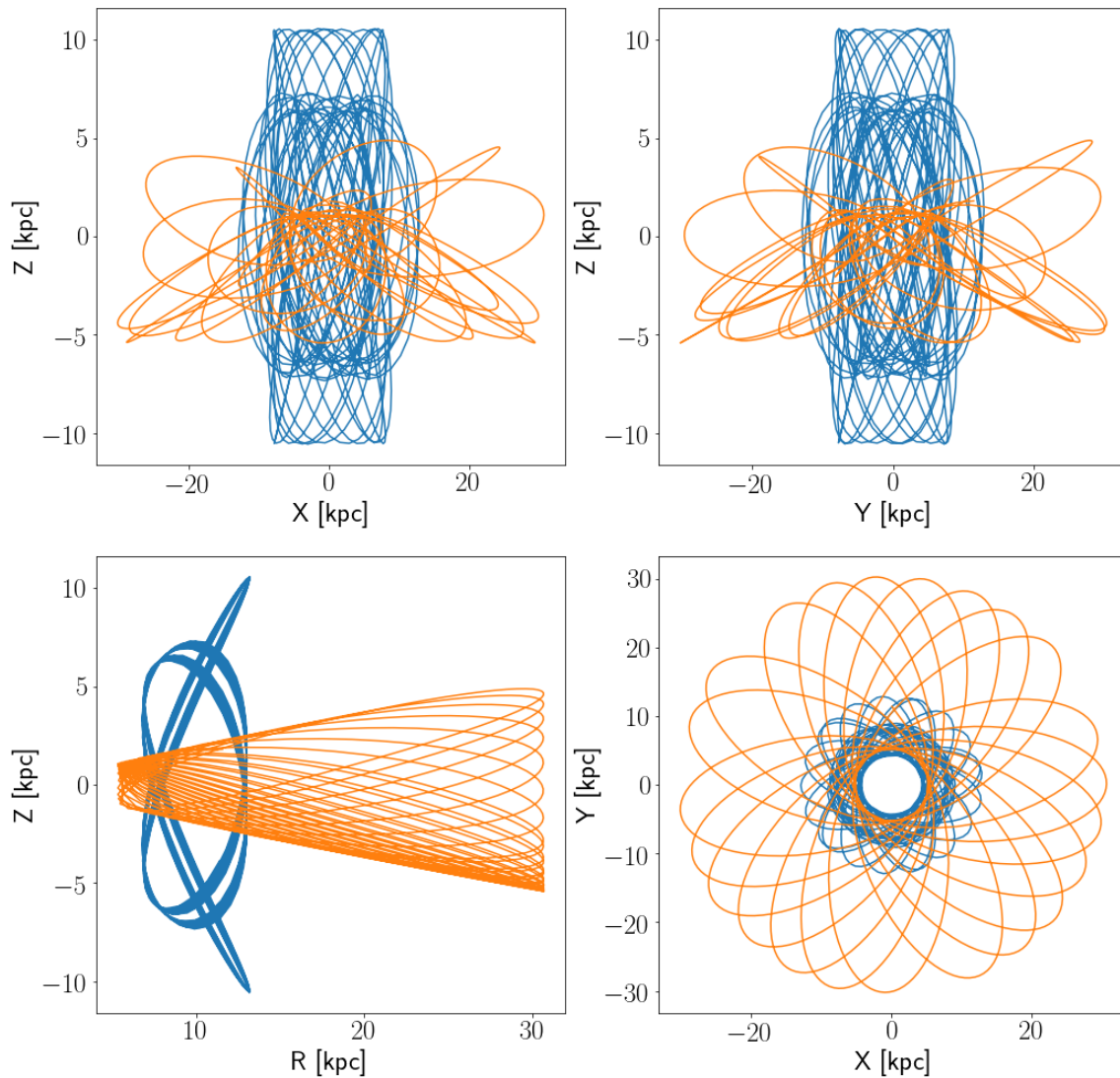


**FIGURE 8** Orbits of the two stars (blue and orange for TYC 622–742–1 and TYC 1193–1918–1, respectively) in various planes in Galactocentric X,Y,Z Cartesian coordinates and in the Galactocentric distance R versus height over the galactic plane Z (lower left panel). Orbits were integrated 10 Gyr backwards.

by Simmerer et al. (2004) who give a  $[C/Fe]$  ratio 0.24 dex higher and BD+01 2916; the star HD 118055 from Gratton et al. (2000); the star HD 6268 from Meléndez & Barbuy (2002), observed also by McWilliam et al. (1995) providing  $[C/Fe]$  0.26 dex larger and by Honda et al. (2004) who derive  $[C/Fe]$  0.43 dex larger; the star WISEJ211458.65–763146.8 by Placco et al. (2019). The stars from the literature and the

two stars here investigated in Fig. 12 are compared to our two stars and the sample by Gratton et al. (2000) and Spite et al. (2005). Such low  $[C/Fe]$  evolved stars are surely rare objects, but still at least a dozen are known, so it could simply be that the C correction suggested by Placco et al. (2014) is too small in the case of luminous stars. But in the literature we could find also unevolved metal-poor stars poor in carbon (see

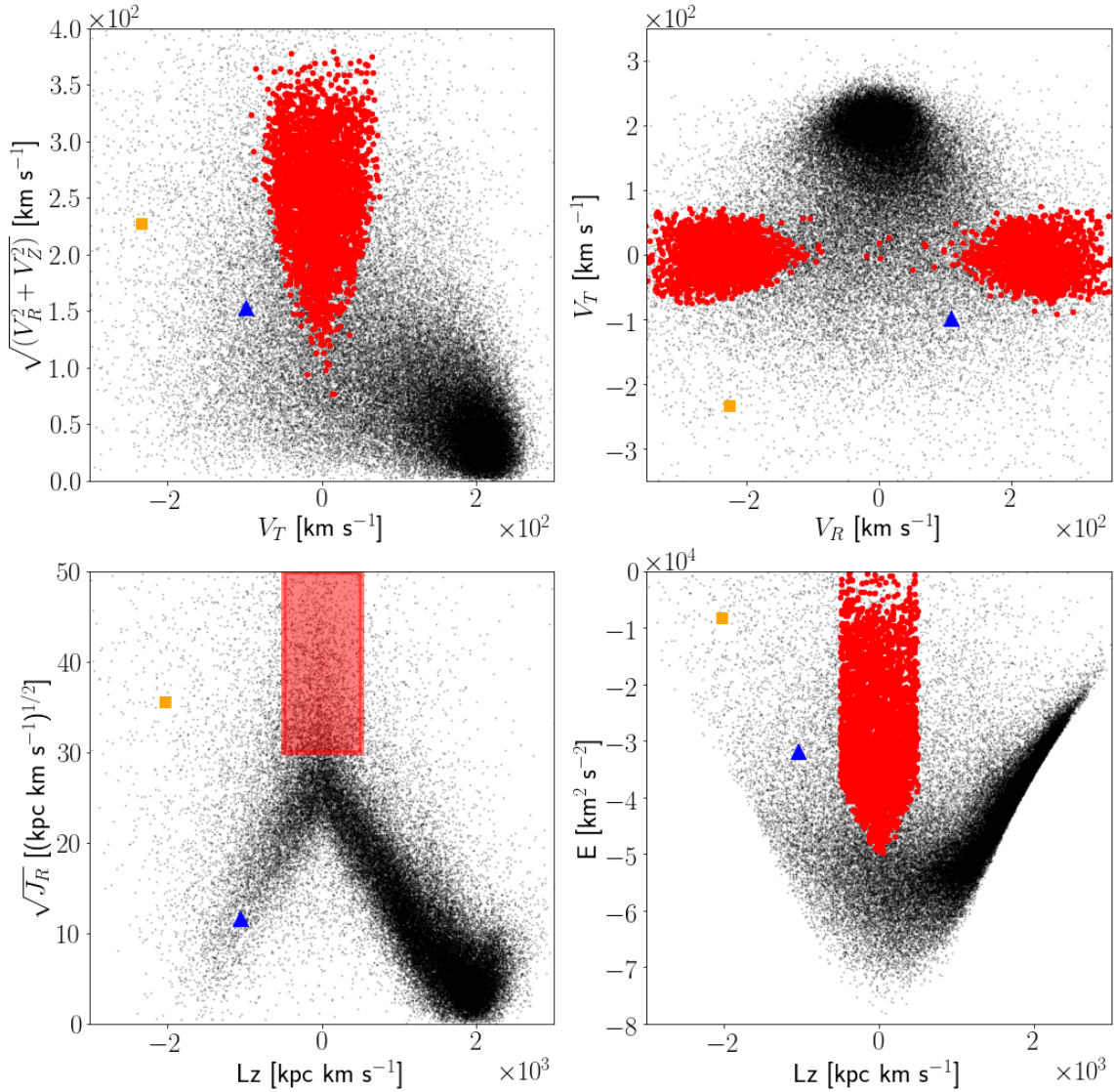


**FIGURE 9** Top panels: position of the target stars (blue triangle and orange square for TYC 622–742–1 and TYC 1193–1918–1, respectively) according to their Galactocentric cylindrical velocities ( $V_T$  vs  $V_R$  and  $\sqrt{V_R^2 + V_Z^2}$  vs  $V_T$  left and right panel, respectively). Bottom panels: position of the target stars in the orbital Energy (right) and  $\sqrt{J_R}$  (left) vs  $L_z$  planes. Stars from the good parallax sample of Bonifacio et al. (2021) are shown as black dots. The red-shaded area in the bottom-left panel outlines the region defined in Feuillet et al. (2020) to select GSE stars. Stars belonging to this area are presented as red filled circles in the other panels.

Aguado et al., 2016; Aoki et al., 2013; Placco et al., 2019). It is then possible that also TYC 622–742–1 was C-poor when it was on the main sequence. We remark here that the spectral lines in TYC 622–742–1 are rather broad, corresponding to a

gaussian broadening of about  $10 \text{ km s}^{-1}$ . The quality of the data does not allow us to distinguish between rotational broadening and macroturbulence broadening. Either way it could be

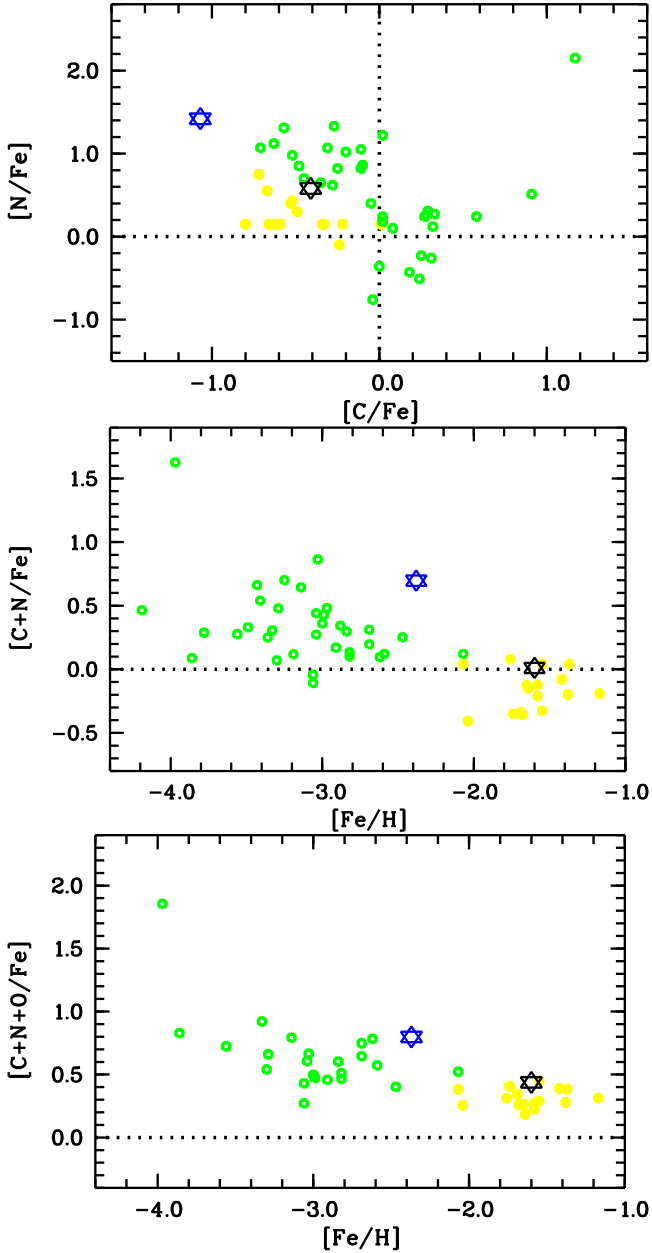


**FIGURE 10**  $[N/Fe]$  vs.  $[C/Fe]$ ,  $[C+N/Fe]$  vs.  $[Fe/H]$  and  $[C+N+O/Fe]$  vs.  $[Fe/H]$  of the two stars compared to the evolved stars from Gratton et al. (2000, yellow dots) sample and stars from Spite et al. (2005, green dots).

that the phenomenon responsible for broadening the lines is also responsible for a more efficient mixing, that brings more nuclearily processed material, with low C and high N, into the atmosphere.

TYC 622–742–1 shows also an enhancement in O, Zr, Pr, Sm. Both stars are: (i) slightly enhanced in Sc; (ii) poor in Y; (iii) rich in Eu. As visible in Fig. 13, the two stars show very similar  $[X/Fe]$  ratios.

## 5 | CONCLUSIONS

We investigated high-quality spectra of two stars selected for their high speed and compared their chemical pattern to literature analyses. We could derive abundances for 28 elements (C, N, O, Na, Mg, Al, Si, Ca, Sc, Ti, V, Cr, Mn, Fe, Co, Ni, Cu, Zn, Sr, Y, Zr, Ba, La, Ce, Pr, Nd, Sm, Eu), and abundances from two ionisation states in the case of four elements (Ti, Cr, Fe and Zr). The two stars are similar in the chemical pattern with respect to Fe (see Fig. 13). From a chemical point of view:

- the two stars are metal-poor;
- both are  $\alpha$ -enhanced;
- both stars are poor in C and rich in N, as expected for evolved stars, and this fact is supported by the low  $^{12}C/^{13}C$  isotopic ratio in TYC 1193–1918–1;
- the stars show a slight excess in Eu abundance.

From a kinematic point of view these are Halo stars not belonging to the GSE structure. These two stars have retrograde orbits with high ellipticity. They display a chemical composition that is, by and large, indistinguishable from that of other halo stars of similar metallicity.

## ACKNOWLEDGMENTS

We gratefully acknowledge support from the French National Research Agency (ANR) funded project “Pristine” (ANR-18-CE31-0017). This work has made use of data from the European Space Agency (ESA) mission *Gaia* (<https://www.cosmos.esa.int/gaia>), processed by the *Gaia* Data Processing and Analysis Consortium (DPAC, <https://www.cosmos.esa.int/web/gaia/dpac/consortium>). Funding for the DPAC has been provided by national institutions, in particular the institutions participating in the *Gaia* Multilateral Agreement. This research has made use of the SIMBAD database, operated at CDS, Strasbourg, France.

## Author contributions

A.M. Matas Pinto analysed the light elements, investigated the NLTE effects, prepared the tables and figures. E. Caffau supervised the analysis, wrote the paper. P. François was the PI of the observing program, observed and reduced the spectra, analysed the heavy elements. M. Spite supervised the analysis. P. Bonifacio selected the targets, derived the stellar parameters, contributed writing the text. S. Wanajo worked on the observing proposal and contributed on the preparation of

the final text. W. Aoki worked on the observing proposal and contributed on the preparation of the final text. L. Monaco computed the kinematic properties and orbits. T. Suda gave fundamental contributions on the C abundance and contributed on the preparation of the final text. F. Spite contributed on the discussion on the results and the preparation of the final text. L. Sbordone provided updates in the pipeline used for the analysis and the model atmospheres used in the chemical investigation. L. Lombardo was involved in the C abundance determination. A. Mucciarelli provided the model atmospheres used in the determinations of the stellar parameters.

## Financial disclosure

None reported.

## Conflict of interest

The authors declare no potential conflict of interests.

## REFERENCES

- Aguado, D. S., Allende Prieto, C., González Hernández, J. I., et al. 2018, *ApJ*, 854, L34. doi:10.3847/2041-8213/aaadb8
- Aguado, D. S., Allende Prieto, C., González Hernández, J. I., et al. 2016, *A&A*, 593, A10. doi:10.1051/0004-6361/201628371
- Alexeeva, S., Ryabchikova, T., Mashonkina, L., et al. 2018, *ApJ*, 866, 153
- Alvarez, R. & Plez, B. 1998, *A&A*, 330, 1109
- Andrés Galarza, C., Daffon, S., Placco, V. M., et al. 2021, *A&A*, in press, arXiv:2109.11600
- Andrievsky, S., Bonifacio, P., Caffau, E., et al. 2018, *MNRAS*, 473, 3377
- Andrievsky, S. M., Spite, F., Korotin, S. A., et al. 2011, *A&A*, 530, A105. doi:10.1051/0004-6361/201116591
- Aoki, W., Suda, T., Boyd, R. N., et al. 2013, *ApJ*, 766, L13. doi:10.1088/2041-8205/766/L13
- Aoki, W. & Honda, S. 2008, *PASJ*, 60, L7. doi:10.1093/pasj/60.3.L7
- Beers, T. C., Preston, G. W., & Shectman, S. A. 1985, *AJ*, 90, 2089. doi:10.1086/113917
- Belokurov, V., Erkal, D., Evans, N. W., et al. 2018, *MNRAS*, 478, 611
- Bergemann, M., Collet, R., Amarsi, A. M., et al. 2017, *ApJ*, 847, 15
- Bergemann, M. & Gehren, T. 2008, *A&A*, 492, 823
- Bergemann, M., Kudritzki, R.-P., Plez, B., et al. 2012, *ApJ*, 751, 156
- Bergemann, M., Lind, K., Collet, R., et al. 2012, *MNRAS*, 427, 27
- Bergemann, M., Kudritzki, R.-P., Würfl, M., et al. 2013, *ApJ*, 764, 115
- Bergemann, M., Pickering, J. C., & Gehren, T. 2010, *MNRAS*, 401, 1334
- Bidelman, W. P. & MacConnell, D. J. 1973, *AJ*, 78, 687. doi:10.1086/111475
- Bond, H. E. 1970, *ApJS*, 22, 117. doi:10.1086/190220
- Bond, H. E. 1980, *ApJS*, 44, 517. doi:10.1086/190703
- Bonifacio, P. & Caffau, E. 2003, *A&A*, 399, 1183
- Bonifacio, P., Spite, M., Cayrel, R., et al. 2009, *A&A*, 501, 519
- Bonifacio, P., Caffau, E., Spite, M., et al. 2015, *A&A*, 579, A28. doi:10.1051/0004-6361/201425266
- Bonifacio, P., Caffau, E., Spite, M., et al. 2018, *A&A*, 612, A65. doi:10.1051/0004-6361/201732320
- Bonifacio, P., Caffau, E., Sestito, F., et al. 2019, *MNRAS*, 487, 3797. doi:10.1093/mnras/stz1378
- Bonifacio, P., Monaco, L., Salvadori, S., et al. 2021, *A&A*, 651, A79. doi:10.1051/0004-6361/202140816
- Bovy, J. 2015, *ApJS*, 216, 29
- Bressan, A., Marigo, P., Girardi, L., et al. 2012, *MNRAS*, 427, 127
- Caffau, E., Ludwig, H.-G., Steffen, M., Freytag, B., & Bonifacio, P. 2011, *Sol. Phys.*, 268, 255
- Caffau, E., Bonifacio, P., Sbordone, L., et al. 2013, *A&A*, 560, A71
- Caffau, E., Bonifacio, P., Spite, M., et al. 2016, *A&A*, 595, L6. doi:10.1051/0004-6361/201629776
- Caffau, E., Bonifacio, P., Sbordone, L., et al. 2020, *MNRAS*, 493, 4677. doi:10.1093/mnras/staa589
- Caffau, E., Monaco, L., Bonifacio, P., et al. 2020, *A&A*, 638, A122.
- Caffau, E., Bonifacio, P., Korotin, S. A., et al. 2021, *A&A*, 651, A20. doi:10.1051/0004-6361/202140808
- Cayrel, R., Depagne, E., Spite, M., et al. 2004, *A&A*, 416, 1117
- Cayrel, R., Hill, V., Beers, T. C., et al. 2001, *Nature*, 409, 691
- Cenarro, A. J., Moles, M., Cristóbal-Hornillos, D., et al. 2019, *A&A*, 622, A176. doi:10.1051/0004-6361/201833036
- Chamberlain, J. W., & Aller, L. H. 1951, *ApJ*, 114, 52
- Charbonnel, C., Lagarde, N., Jasniewicz, G., et al. 2020, *A&A*, 633, A34. doi:10.1051/0004-6361/201936360
- Christlieb, N., Schörck, T., Frebel, A., et al. 2008, *A&A*, 484, 721. doi:10.1051/0004-6361:20078748
- Christlieb, N., Reimers, D., & Wisotzki, L. 2004, *The Messenger*, 117, 40
- Christlieb, N., Bessell, M. S., Beers, T. C., et al. 2002, *Nature*, 419, 904. doi:10.1038/nature01142
- Christlieb, N., Reimers, D., Wisotzki, L., et al. 2000, *The First Stars*, 49. doi:10.1007/10719504\_6
- Cui, X.-Q., Zhao, Y.-H., Chu, Y.-Q., et al. 2012, *Research in Astronomy and Astrophysics*, 12, 1197. doi:10.1088/1674-4527/12/9/003
- Di Matteo, P., Haywood, M., Lehnert, M. D., et al. 2019, *A&A*, 632, A4
- Feuillet, D. K., Feltzing, S., Sahlholdt, C. L., et al. 2020, *MNRAS*, 497, 109. doi:10.1093/mnras/staa1888
- Fulbright, J. P. 2000, *AJ*, 120, 1841
- Gaia Collaboration, Prusti, T., de Bruijne, J. H. J., et al. 2016, *A&A*, 595, A1
- Gaia Collaboration, Brown, A. G. A., Vallenari, A., et al. 2018, *A&A*, 616, A1
- Gaia Collaboration, Brown, A. G. A., Vallenari, A., et al. 2021, *A&A*, 649, A1. doi:10.1051/0004-6361/202039657
- Gallagher, A. J., Caffau, E., Bonifacio, P., et al. 2016, *A&A*, 593, A48
- González Hernández, J. I. & Bonifacio, P. 2009, *A&A*, 497, 497. doi:10.1051/0004-6361/200810904
- Gratton, R. G., Snenen, C., Carretta, E., et al. 2000, *A&A*, 354, 169
- Hansen, T. T., Holmbeck, E. M., Beers, T. C., et al. 2018, *ApJ*, 858, 92. doi:10.3847/1538-4357/aabacc
- Haywood, M., Di Matteo, P., Lehnert, M. D., et al. 2018, *ApJ*, 863, 113
- Heiter, U., Lind, K., Bergemann, M., et al. 2021, *A&A*, 645, A106. doi:10.1051/0004-6361/201936291
- Helmi, A., Babusiaux, C., Koppelman, H. H., et al. 2018, *Nature*, 563, 85
- Henden, A. A., Welch, D. L., Terrell, D., & Levine, S. E. 2009, *American Astronomical Society Meeting Abstracts #214*, 214, 407.02
- Honda, S., Aoki, W., Kajino, T., et al. 2004, *ApJ*, 607, 474. doi:10.1086/383406

- Ishigaki, M. N., Chiba, M., & Aoki, W. 2012, *ApJ*, 753, 64.
- Ishigaki, M. N., Aoki, W., & Chiba, M. 2013, *ApJ*, 771, 67.
- Jacobson, H. R., Keller, S., Frebel, A., et al. 2015, *ApJ*, 807, 171. doi:10.1088/0004-637X/807/2/171
- Keller, S. C., Schmidt, B. P., Bessell, M. S., et al. 2007, *PASA*, 24, 1. doi:10.1071/AS07001
- Korn, A. J., Shi, J., & Gehren, T. 2003, *A&A*, 407, 691
- Korotin, S. A., Andrievsky, S. M., Hansen, C. J., et al. 2015, *A&A*, 581, A70
- Kurucz, R. L. 2005, *Memorie della Societa Astronomica Italiana Supplementi*, 8, 14
- Li, H. N., Ludwig, H.-G., Caffau, E., et al. 2013, *ApJ*, 765, 51. doi:10.1088/0004-637X/765/1/51
- Li, H., Aoki, W., Zhao, G., et al. 2015, *PASJ*, 67, 84. doi:10.1093/pasj/psv053
- Li, H.-N., Zhao, G., Christlieb, N., et al. 2015, *ApJ*, 798, 110. doi:10.1088/0004-637X/798/2/110
- Li, H., Tan, K., & Zhao, G. 2018, *ApJS*, 238, 16. doi:10.3847/1538-4365/aada4a
- Lindgren, L., Klioner, S. A., Hernández, J., et al. 2021, *A&A*, 649, A2. doi:10.1051/0004-6361/202039709
- Lodders, K., Palme, H., & Gail, H.-P. 2009, *Landolt Börnstein*, 712
- Marigo, P., Girardi, L., Bressan, A., et al. 2017, *ApJ*, 835, 77
- Mashonkina, L. I., Sitnova, T. N., & Pakhomov, Y. V. 2016, *Astronomy Letters*, 42, 606
- Mashonkina, L., Jablonka, P., Pakhomov, Y., et al. 2017, *A&A*, 604, A129
- Masseron, T., Plez, B., Van Eck, S., et al. 2014, *A&A*, 571, A47
- Matijević, G., Chiappini, C., Grebel, E. K., et al. 2017, *A&A*, 603, A19. doi:10.1051/0004-6361/201730417
- Matsuno, T., Aoki, W., & Suda, T. 2019, *ApJ*, 874, L35. doi:10.3847/2041-8213/ab0ec0
- Matsuno, T., Aoki, W., Beers, T. C., et al. 2017, *AJ*, 154, 52. doi:10.3847/1538-3881/aa7a08
- McWilliam, A., Preston, G. W., Sneden, C., et al. 1995, *AJ*, 109, 2757. doi:10.1086/117486
- Meléndez, J. & Barbuy, B. 2002, *ApJ*, 575, 474. doi:10.1086/341142
- Mendes de Oliveira, C., Ribeiro, T., Schoenell, W., et al. 2019, *MNRAS*, 489, 241. doi:10.1093/mnras/stz1985
- Monaco, L., Bellazzini, M., Bonifacio, P., et al. 2005, *A&A*, 441, 141
- Mucciarelli, A., Bellazzini, M., & Massari, D. 2021, *A&A*, in press, doi:10.1051/0004-6361/202140979
- Nissen, P. E., Hoeg, E., & Schuster, W. J. 1997, *Hipparcos - Venice '97*, 402, 225
- Nordlander, T. & Lind, K. 2017, *A&A*, 607, A75
- Noguchi, K., Aoki, W., Kawanomoto, S. et al. 2002, *PASJ*, 54, 855
- Placco, V. M., Santucci, R. M., Beers, T. C., et al. 2019, *ApJ*, 870, 122. doi:10.3847/1538-4357/aaf3b9
- Placco, V. M., Frebel, A., Beers, T. C., et al. 2014, *ApJ*, 797, 21. doi:10.1088/0004-637X/797/1/21
- Placco, V. M., Roederer, I. U., Lee, Y. S., et al. 2021, *ApJ*, 912, L32. doi:10.3847/2041-8213/abf93d
- Price-Whelan, A. 2018, *Zenodo*
- Raddi, R., Irrgang, A., Heber, U., et al. 2021, *A&A*, 645, A108. doi:10.1051/0004-6361/202037872
- Roman, N. G. 1955, *ApJS*, 2, 195. doi:10.1086/190021
- Roman, N. G. 1950, *ApJ*, 112, 554. doi:10.1086/145367
- Salaris, M. & Weiss, A. 2001, *A&A*, 376, 955. doi:10.1051/0004-6361:20010982
- Sbordone, L., Caffau, E., Bonifacio, P., & Duffau, S. 2014, *A&A*, 564, A109
- Schlafly, E. F., & Finkbeiner, D. P. 2011, *ApJ*, 737, 103
- Schlaufman, K. C. & Casey, A. R. 2014, *ApJ*, 797, 13. doi:10.1088/0004-637X/797/1/13
- Schönrich, R., Binney, J., & Dehnen, W. 2010, *MNRAS*, 403, 1829
- Schwarzschild, M. & Schwarzschild, B. 1950, *ApJ*, 112, 248. doi:10.1086/145340
- Simmerer, J., Sneden, C., Cowan, J. J., et al. 2004, *ApJ*, 617, 1091. doi:10.1086/424504
- Sitnova, T. M., Mashonkina, L. I., & Ryabchikova, T. A. 2013, *Astronomy Letters*, 39, 126
- Skúladóttir, Á., Hansen, C. J., Salvadori, S., et al. 2019, *A&A*, 631, A171
- Spite, M., Cayrel, R., Plez, B., et al. 2005, *A&A*, 430, 655
- Spite, M., Andrievsky, S. M., Spite, F., et al. 2012, *A&A*, 541, A143
- Starkenburger, E., Aguado, D. S., Bonifacio, P., et al. 2018, *MNRAS*, 481, 3838. doi:10.1093/mnras/sty2276
- Starkenburger, E., Martin, N., Youakim, K., et al. 2017, *MNRAS*, 471, 2587. doi:10.1093/mnras/stx1068
- Steinmetz, M., Zwitter, T., Siebert, A., et al. 2006, *AJ*, 132, 1645. doi:10.1086/506564
- Suda, T., Katsuta, Y., Yamada, S., et al. 2008, *PASJ*, 60, 1159. doi:10.1093/pasj/60.5.1159
- Takeda, Y., Zhao, G., Takada-Hidai, M., et al. 2003, *Chinese J. Astron. Astrophys.*, 3, 316
- Tonry, J. & Davis, M. 1979, *AJ*, 84, 1511. doi:10.1086/112569
- Valentini, M., Chiappini, C., Bossini, D., et al. 2019, *A&A*, 627, A173
- Whitten, D. D., Placco, V. M., Beers, T. C., et al. 2021, *ApJ*, 912, 147. doi:10.3847/1538-4357/abee7e
- Wolf, C., Onken, C. A., Luvaul, L. C., et al. 2018, *PASA*, 35, e010. doi:10.1017/pasa.2018.5
- York, D. G., Adelman, J., Anderson, J. E., et al. 2000, *AJ*, 120, 1579



## APPENDIX A: ATOMIC DATA

The atomic data are provided in a table deposited to CDS and here below in Table A1 – the first lines are shown. In the Table we list the atomic lines used of [OI], Na I, Mg I, Al I, Si I, Ca I, Sc II, Ti I, Ti II, V I, Cr I, Cr II, Mn I, Fe II, Co I, Ni I, Cu I, Zn I, Sr II, Y II, Zr I, Zr II, Ba II, La II, Ce II, Pr II, Nd II, Sm II, Eu II. The atomic data are from Heiter et al. (2021). Hyperfine splitting has been taken into account when deriving the abundances of the following elements V, Mn, Co, Cu, Ba, Pr, Nd, Eu, but is not listed below. The solar mix isotopic ratios provided in Table 3 of Heiter et al. (2021) have been used for the computation of the abundances.

**TABLE A1** Atomic data.

Star	Element Z ion	Wavelength [nm]	loggf	LowerEnergy [cm-1]
TYC 622-742-1	8 0	630.0304	-9.715	0.000
TYC 622-742-1	8 0	636.3776	-10.190	161.311
TYC 1193-1918-1	8 0	636.3776	-10.190	161.311
TYC 622-742-1	11 0	498.2814	-0.916	16969.908
TYC 622-742-1	11 0	568.2633	-0.706	16953.775
TYC 622-742-1	11 0	568.8205	-0.404	16969.908
TYC 1193-1918-1	11 0	498.2814	-0.916	16969.908
TYC 1193-1918-1	11 0	568.2633	-0.706	16953.775
TYC 1193-1918-1	11 0	568.8205	-0.404	16969.908
TYC 1193-1918-1	11 0	589.5924	-0.144	0.000
TYC 1193-1918-1	11 0	616.0747	-1.246	16969.908
TYC 622-742-1	12 0	470.2991	-0.440	35052.859
TYC 622-742-1	12 0	552.8405	-0.498	35052.859
TYC 622-742-1	12 0	571.1088	-1.724	35052.859
TYC 1193-1918-1	12 0	470.2991	-0.440	35052.859
TYC 1193-1918-1	12 0	552.8405	-0.498	35052.859

These are only a few lines of the full table.

The full table is made available both as supporting online material on the journal's web page and at CDS <https://cdsarc.cds.unistra.fr/viz-bin/cat/J/AN/Vol/Page/>

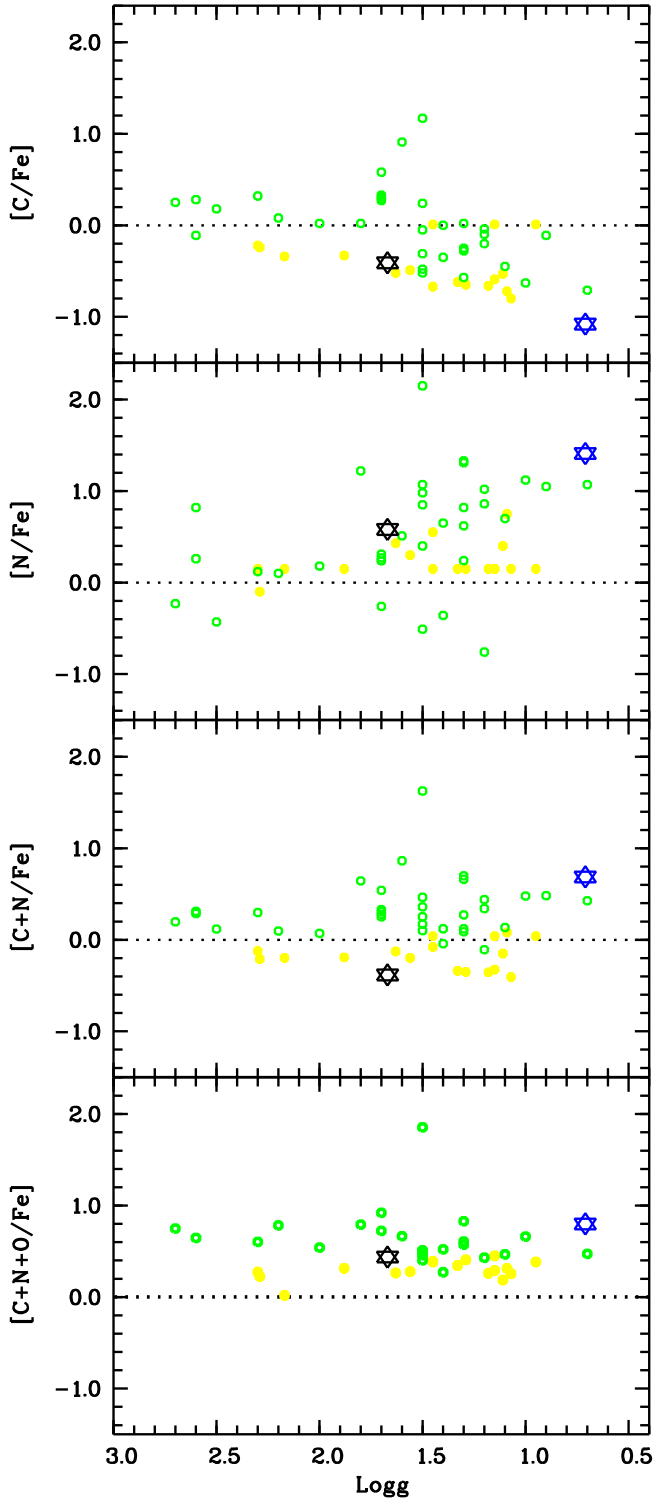


**FIGURE 11**  $[C/Fe]$ ,  $[N/Fe]$ ,  $[C+N/Fe]$  and  $[C+N+O/Fe]$  vs.  $\log g$  of the two stars compared to the evolved stars from Gratton et al. (2000, yellow dots) sample and stars from Spite et al. (2005, green dots).

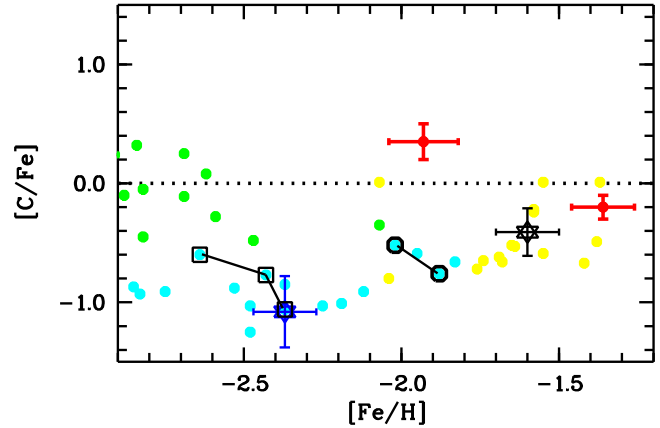


**FIGURE 12**  $[C/Fe]$  vs.  $[Fe/H]$  of the two stars compared to the evolved stars from the literature: Gratton et al. (2000, yellow dots), Spite et al. (2005, green dots) and from the database Suda et al. (2008, light blue dots). The star HD 6268 (light blue dots surrounded by black squares) has three independent analysis, one of which gave results very similar to TYC 622–742–1 and HD 29574 (light blue dots surrounded by black circles).

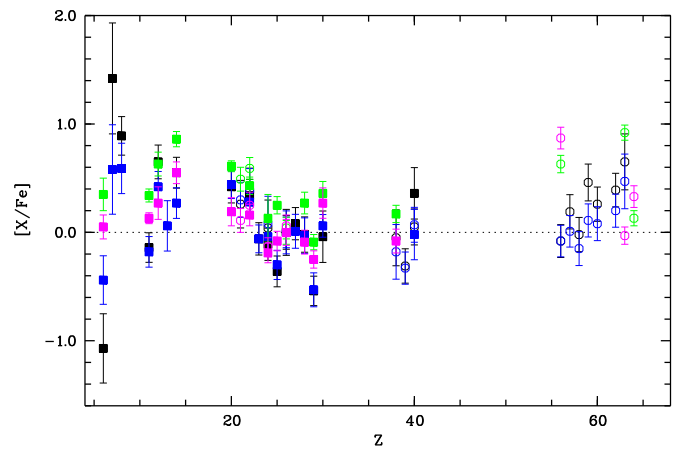


**FIGURE 13** The chemical pattern of TYC 622–742–1 (black circles) and TYC 1193–1918–1 (blue circles) compared to the two high-speed stars in Valentini et al. (2019) (green and pink circles). Full symbols are used to show abundances derived from neutral lines and empty symbols from ionised lines.